The Astronomical Journal, 171:314 (20pp), 2026 May
https://doi.org/10.3847/1538-3881/ae5b9f

Supersolar Metallicity and Tentative Evidence for Photochemistry on WASP-96 b from JWST and Ground-based VLT Transmission Spectroscopy

Michael Radica[1,2,16], Jake Taylor[3], Yoav Rotman[4], Jasmina Blecic[5,6], Luis Welbanks[4], Eva-Maria Ahrer[7], Duncan Christie[7], Louis-Philippe Coulombe[2,8], Gillis Lowry[9,10], Matthew M. Murphy[11], Adina D. Feinstein[12], David Lafrenière[2], Ryan J. MacDonald[13], Nathan J. Mayne[14], Shang-Min Tsai[15], and Maria Zamyatina[14]
[1] Department of Astronomy & Astrophysics, University of Chicago, 5640 South Ellis Avenue, Chicago, IL 60637, USA; radicamc@uchicago.edu
[2] Institut Trottier de Recherche sur les Exoplanètes, 1375 Avenue Thérèse-Lavoie-Roux, Montréal, QC, H2V 0B3, Canada
[3] Department of Physics, University of Oxford, Parks Road, Oxford OX1 3PU, UK
[4] School of Earth and Space Exploration, Arizona State University, Tempe, AZ, USA
[5] Department of Physics, New York University Abu Dhabi, Abu Dhabi, UAE
[6] Center for Astrophysics and Space Science (CASS), New York University Abu Dhabi, Abu Dhabi, UAE
[7] Max Planck Institute for Astronomy, Königstuhl 17, D-69117 Heidelberg, Germany
[8] Planétarium de Montréal, Espace pour la Vie, 4801 av. Pierre-de Coubertin, Montréal, Canada
[9] Carl Sagan Institute, Cornell University, 302 Space Sciences Building, Ithaca, NY 14853, USA
[10] Department of Physics & Astronomy, San Francisco State University, 1600 Holloway Avenue, San Francisco, CA 94132, USA
[11] Department of Physics and Astronomy, Michigan State University, East Lansing, MI, USA
[12] Department of Physics and Astronomy, Michigan State University, East Lansing, MI 48824, USA
[13] School of Physics & Astronomy, University of St Andrews, North Haugh, St. Andrews, KY16 9SS, UK
[14] Department of Physics and Astronomy, Faculty of Environment, Science and Economy, University of Exeter, Exeter EX4 4QL, UK
[15] Institute of Astronomy & Astrophysics, Academia Sinica, Taipei 10617, Taiwan

Received 2025 December 19; revised 2026 March 15; accepted 2026 April 3; published 2026 April 27

Abstract

With its expanded wavelength coverage and increased precision compared to previous space-based observatories, JWST provides the opportunity to revisit benchmark planets and view them in a new light. Here, we conduct an in-depth study of the atmosphere of the hot-Saturn WASP-96 b combining a new JWST NIRSpec/G395H transit with archival NIRISS/SOSS and Very Large Telescope/FORS2 transmission spectra. The combined spectrum shows clearly visible features from H_2O, CO_2, and Na. CO, though, remains unconstrained, precluding a firm metallicity derivation from free retrievals alone. However, self-consistent grids yield a broadly superstellar atmospheric metallicity of 2–6× stellar. When combined with a roughly stellar C/O ratio ($0.41^{+0.10}_{-0.09}$ from self-consistent grids), we find that WASP-96 b potentially formed via core-accretion beyond the H_2O snowline and subsequently accreted volatile-rich material. Free retrievals also find a moderate preference ($\ln B = 2.69$) for models with SO_2 versus without. WASP-96 b falls directly on the proposed "SO_2 shoreline" and the retrieved SO_2 abundance is well-matched to predictions from photochemical models. Our combined spectrum displays an optical slope, which our models fit with opacity from scattering aerosols—either small-particle condensate clouds or photochemical hazes—though we cannot completely rule out the broad wings of Na or the effects of stellar contamination. Future observations are necessary to disentangle these effects. Finally, we explore the possibility for limb asymmetry in WASP-96 b's transmission spectrum and provide several tests to identify asymmetries in our data. We encourage the community to prioritize the development of a robust pathway to quantify the presence of limb asymmetry—particularly for low signal-to-noise cases.

Unified Astronomy Thesaurus concepts: Exoplanets (498); Exoplanet atmospheres (487); Planetary atmospheres (1244)

1. Introduction

The study of exoplanet atmospheres is now in an era of unprecedented observational sensitivity and precision, particularly due to JWST. Since the start of science operations in mid-2022, the community has leveraged the capabilities of JWST to access regimes not readily available to previous observatories: in-depth searches for atmospheres around rocky worlds (e.g., T. P. Greene et al. 2023; E. M. May et al. 2023; S. E. Moran et al. 2023; O. Lim et al. 2023; S. Zieba et al. 2023; M. Zhang et al. 2024; M. Radica et al. 2025b) and investigations into the natures of sub-Neptunes (e.g., E. M.-R. Kempton et al. 2023; N. Madhusudhan et al. 2023; B. Benneke et al. 2024; C. Piaulet-Ghorayeb et al. 2024; E.-M. Ahrer et al. 2025a; B. Davenport et al. 2025) being prime examples.

Although JWST has certainly opened up many new observational regimes ripe for exploration, it is also important to turn its powers to the atmospheres of giant planets. The high temperatures and large radii of hot Jupiters and Saturns render their atmospheres easily observable (S. Seager & D. D. Sasselov 2000; E. M.-R. Kempton et al. 2018). Beyond sheer observability, though, transit spectroscopy of hot gas giants presents an incredible, high signal-to-noise ratio (S/N) laboratory to study the myriad processes that govern planetary atmospheres: from photochemistry and other disequilibrium processes (J. I. Moses et al. 2011; S.-M. Tsai et al. 2023; G. Fu et al. 2024; L. Welbanks et al. 2024; I. J. M. Crossfield et al.

---

[16] NSERC Postdoctoral Fellow.

2025; S. Mukherjee et al. 2025a), to atmosphere escape (M. Mansfield et al. 2018; J. J. Spake et al. 2018; R. Allart et al. 2025; V. Krishnamurthy et al. 2025), cloud formation (H. R. Wakeford et al. 2017; D. Grant et al. 2023; A. Dyrek et al. 2024), and the impacts of planetary formation and migration (e.g., K. I. Öberg et al. 2011; N. Madhusudhan et al. 2014; A. B. T. Penzlin et al. 2024; E.-M. Ahrer et al. 2025b).

Recently, we have also begun to identify differences in the morning and evening limb transmission spectra of giant planets with JWST (i.e., limb asymmetries; N. Espinoza et al. 2024; M. M. Murphy et al. 2024b, 2025; S. Mukherjee et al. 2025b). Although limb asymmetries have been detected at high resolution from the ground (e.g., D. Ehrenreich et al. 2020; S. Gandhi et al. 2022), such observations were out of reach for previous space-based instruments due to strong systematics and noncontinuous observations. It is, therefore, still pertinent to revisit benchmark planets from the Hubble Space Telescope (HST) era to see what JWST can reveal about them.

WASP-96 b, an inflated hot-Saturn ($M{\sim}0.48\,M_{\rm Jup}$, $R \sim 1.2\,R_{\rm Jup}$; C. Hellier et al. 2014), is one such benchmark world. It was the target of transit observations with Very Large Telescope (VLT)/FORS2 (0.36–0.82 μm) by N. Nikolov et al. (2018), as well as with the Wide Field Camera 3 (WFC3) instrument on HST (1.1–1.7 μm) and the Spitzer Space Telescope's Infrared Array Camera (IRAC) by N. K. Nikolov et al. (2022), leading to claims of an aerosol-free (i.e., cloud and haze free) terminator atmosphere—mostly due to the highly broadened wings of the Na feature visible in the FORS2 spectrum (N. Nikolov et al. 2018; N. K. Nikolov et al. 2022). Although a follow-up Magellan/IMACS (0.44–0.97 μm) transit spectrum by C. D. McGruder et al. (2022) did not show the broad Na wings as clearly as VLT/FORS2, and K. H. Yip et al. (2021) highlighted the difficulties in combining space- and ground-based datasets, both studies also supported the aerosol-free interpretation of WASP-96 b's transmission spectrum. N. K. Nikolov et al. (2022) also conducted an in-depth chemical analysis of WASP-96 itself and, combined with their transmission spectra, found stellar-to-superstellar abundances of O and Na in the atmosphere of WASP-96 b.

WASP-96 b was then targeted with the Near Infrared Imager and Slitless Spectrograph (NIRISS; R. Doyon et al. 2023) on JWST as part of the Early Release Observations program. M. Radica et al. (2023) and J. Taylor et al. (2023) analyzed one transit using the Single Object Slitless Spectroscopy (SOSS; L. Albert et al. 2023) mode, covering wavelengths 0.6–2.85 μm. They noted the presence of a short-wavelength slope in the continuous SOSS spectrum, which could potentially be masked by offsets when stitching together spectra from different instruments (K. H. Yip et al. 2021). As demonstrated by previous work on model degeneracies (e.g., L. Welbanks & N. Madhusudhan 2019), J. Taylor et al. (2023) found that the slope in the optical could be explained either by wings of a highly broadened Na feature, or a scattering aerosol slope—favoring the latter interpretation as general circulation models (GCMs) without aerosol opacity failed to provide an adequate fit to the data. J. Taylor et al. (2023) also concluded that the chemical composition of WASP-96 b was roughly consistent with a solar metallicity atmosphere in chemical equilibrium, with potential indications of enhanced CO_2 and Na abundances (of roughly 10× solar).

This apparent discrepancy between the solar H_2O abundances and supersolar CO_2 abundances was explored by Y. Rotman et al. (2025). Their analysis of the NIRISS spectrum of WASP-96 b, using more flexible nonparametric models, suggest that the uncertainty on previously reported chemical abundances may be underestimated. The revised CO_2 abundance from Y. Rotman et al. (2025) was consistent with expectations from solar and supersolar atmospheric metallicities.

More recently, L.-C. Wang et al. (2026) reanalyzed the NIRISS/SOSS transit and combined the resulting transmission spectrum with published VLT, HST, and Spitzer data. They revise the metallicity, via the H_2O abundance, downwards to substellar values (assuming chemical equilibrium) and also find evidence for a gray cloud deck muting spectral features. In contrast to M. Radica et al. (2023) and J. Taylor et al. (2023) though, they do not find evidence for a possible scattering slope. L.-C. Wang et al. (2026) also claim evidence for a ∼50 s transit time offset in the Na feature, potentially indicating the presence of limb asymmetry.

In this work we conduct a thorough reinterpretation of WASP-96 b's transmission spectra, including in the analysis a new transit with JWST's Near Infrared Spectrograph (NIRSpec; S. M. Birkmann et al. 2022). This adds near-infrared (NIR) wavelength coverage from 3–5 μm, providing access to critical molecules like CO_2, CO, and SO_2 and allowing for a more comprehensive dive into the atmospheric composition of this benchmark giant planet. We present our analysis as follows: Section 2 outlines the observations and data analysis, and Section 3 the atmosphere models that we employ. We then describe our findings on the atmosphere composition of WASP-96 b in Section 4, as well as evidence for and implications of limb asymmetry in Section 5, before concluding in Section 6.

2. Observations and Data Analysis

2.1. JWST NIRSpec/G395H

We observed one transit of WASP-96 b with JWST NIRSpec[17] in BOTS mode (S. M. Birkmann et al. 2022) using the G395H grating (∼2.9–5.0 μm; $R{\sim}3000$). The time series observations (TSO) started on 2024 August 10, at 02:37 UTC and lasted 4.9 hr (using 128 groups and 152 integrations), which captured the 2.4 hr transit and 2.5 hr of baseline observations before and after.

We reduced the data with the widely used `exoTEDRF` pipeline (A. D. Feinstein et al. 2023; M. Radica et al. 2023; M. Radica 2024a), closely following the procedures developed for NIRSpec/G395H observations in, e.g., E.-M. Ahrer et al. (2025a) and R. Luque et al. (2025). This includes subtracting a self-calibrated superbias frame created via an average of the first groups of every integration, group-level $1/f$ correction, linearity correction, time-domain outlier rejection via the algorithm developed in M. Radica et al. (2024), and ramp fitting. We then resubtract the background and any residual $1/f$ noise after ramp fitting, interpolate bad pixels, and trace the spectrum on both the NRS1 and NRS2 detectors using the `edgetrigger` algorithm (M. Radica et al. 2022a), which is well suited to the curved traces of various instruments (e.g., M. Radica et al. 2025a).

---

[17] GO 4082, PI: Radica.

We also apply the principal component analysis (PCA) step commonly employed for SOSS observations (L.-P. Coulombe et al. 2023, 2025; M. Radica et al. 2024), and recently for MIRI (N. J. Connors et al. 2025; R. Luque et al. 2025), to identify potential detector-correlated trends in the data. This analysis identifies a subpixel y-position drift on both detectors over the course of the time series.[18] However, instead of just using this eigenvalue time series as a light curve detrending vector, we use the power of PCA to reconstruct the entire TSO dataset removing this component. This novel analysis step is reminiscent of techniques used to remove telluric contamination in high-resolution observations (e.g., S. Pelletier et al. 2021, 2023) and ensures that the undesired detector-correlated noise is entirely removed from the data prior to light curve fitting. Of course, this analysis can only remove noise sources correlated with detector trends, meaning that any other source of astrophysical noise will still be present in the light curves. We find that removing this subpixel y-position drift from the observations results in a modest reduction of the white light curve scatter (∼10 ppm, or ∼7%).

Finally, we extract the stellar spectra using a simple box aperture with a full width of eight pixels. We explore tweaking several of these reduction steps (e.g., using the default STScI superbias reference file, optimal extraction) and find negligible difference in the end transmission spectrum.

2.2. JWST NIRISS/SOSS

We combine the NIRSpec observations with archival NIRISS/SOSS observations taken as part of the JWST Early Release Observations program. These data were originally presented in M. Radica et al. (2023) with further analysis in J. Taylor et al. (2023). However, we believe it prudent to rereduce the raw data, thereby allowing us to incorporate the approximately 2 yr of advances in JWST data analysis since the original publication.

To that end, we again apply the `exoTEDRF` pipeline to these data, closely following the steps laid out in M. Radica et al. (2024) and M. Radica et al. (2025b). Notable changes to the analysis compared to that of M. Radica et al. (2023) include separate pre- and poststep background scaling (O. Lim et al. 2023; M. Fournier-Tondreau et al. 2024), use of the time-domain outlier rejection instead of the standard up-the-ramp flagging offered by the STScI pipeline, more robust masking of background contaminants during the group-level $1/f$ correction, and the application of the PCA reconstruction step described above. For this, we remove three components identified by the PCA: a subpixel y-position drift, the beating pattern linked to the telescope thermal control (L. Albert et al. 2023), as well as the minor tilt event noted by M. Radica et al. (2023). We also extract the stellar spectra using a simple box aperture with a width of 30 pixels, which we find minimizes the white light curve scatter, instead of the `ATOCA` algorithm (A. Darveau-Bernier et al. 2022) since M. Radica et al. (2023) demonstrated that the effects of the SOSS order self-contamination is indeed negligible for this dataset.

Finally, we apply the post-processing steps described in Section 2.2.4 of M. Radica et al. (2023), the efficacy of which was recently validated by Y. Rotman et al. (2025), to undo the dilution caused by two background contaminants that intersect the target trace.

2.3. Refining WASP-96b's Orbital Solution

A goal of this study is to identify and characterize potential limb differences in WASP-96 b's atmosphere. Since limb differences can be highly degenerate with the transit parameters themselves (e.g., T_0; N. Espinoza & K. Jones 2021; M. M. Murphy et al. 2024a; G. Fu et al. 2025), it is imperative to obtain the most accurate possible orbital solution for WASP-96 b before embarking on this endeavor.

To this end, we supplement our four JWST light curves (two NIRISS/SOSS orders and two NIRSpec detectors) with publicly available light curves from the Transiting Exoplanet Survey Satellite (TESS; G. R. Ricker et al. 2014) and CORALIE radial velocity (RV) measurements from C. Hellier et al. (2014). For TESS, we use the Pre-search Data Conditioning Simple Aperture Photometry (J. M. Jenkins et al. 2016) products from sectors 2 and 29 available from the MAST archive. We do not include the HST light curves from N. K. Nikolov et al. (2022) as their large gaps render them nonideal for constraining orbital properties, nor the VLT or Magellan light curves as they are not publicly available. We convert all timestamps to MJD using routines in the `astropy.Time` library.

We use the flexible `juliet` package (N. Espinoza et al. 2019) to jointly fit the transit and RV datasets. The transit model uses `batman` (L. Kreidberg 2015), assuming a circular orbit (C. Hellier et al. 2014) and with the orbital period, P, midtransit time (fixed to be that of the NIRISS/SOSS transit), T_0, scaled planet radius, R_p/R_*, impact parameter, b, scaled semimajor axis, a/R_*, and the two parameters of the D. M. Kipping (2013) parameterization of the quadratic limb-darkening law, q_1 and q_2, as free parameters. For each JWST dataset, we also include a linear slope with time as a systematics model. The RV fit calls the Keplerian solution from `radvel` (B. J. Fulton et al. 2018), with the RV offset and semiamplitude as additional free parameters. The orbital parameters (i.e., P, T_0, a/R_*, b) are shared between all data, and the rest fit individually to a given dataset as appropriate. An error inflation term is also fit to each dataset, added in quadrature to the errors such that the final reduced χ^2 of the fit is unity. All parameters use wide, uninformative priors except the period to which we give a Gaussian prior based off of the transit timing analysis of A. Kokori et al. (2023). Priors and best-fitting values for relevant parameters are included in Table 1 and the best-fitting models for each dataset are shown in Figure 1.

Our refined orbital parameters are generally consistent with those previously presented in the literature (e.g., C. Hellier et al. 2014; C. D. McGruder et al. 2022; N. K. Nikolov et al. 2022; J. A. Patel & N. Espinoza 2022). In particular our scaled semimajor axis and impact parameter are consistent within errors to the values derived by N. K. Nikolov et al. (2022) using HST, Spitzer, TESS, and ground-based data, as well as J. A. Patel & N. Espinoza (2022) using TESS. However, our precision is higher due in large part to the JWST transits enabling precise constraints on the transit duration from which these parameters are derived (e.g., S. Seager & G. Mallen-Ornelas 2003; A. L. Carter et al. 2024). The consistency in the

---

[18] Several diagnostic plots from the data analysis including the PCA outputs are included in this Zenodo repository: DOI: 10.5281/zenodo.17065171. Hereafter, whenever a Zenodo repository is referred to, it is always this one.

Table 1
Best-fitting Transit Parameters from the Joint Transit and RV Fit

Parameter	Prior Range	Value
Per [day]	$\mathcal{N}[3.42525674, 0.1]$	$3.4252564^{+0.0000002}_{-0.0000002}$
$T0_{SOSS}$ [MJD]	$\mathcal{U}[T0\pm2\ \mathrm{hr}]$	$59751.32470^{+0.00003}_{-0.00003}$
$T0_{NRS}$ [MJD]	$\mathcal{U}[T0\pm2\ \mathrm{hr}]$	$60532.28316^{+0.00003}_{-0.00003}$
Rp/Rs $_{\mathrm{TESS}}$	$\mathcal{U}[0.01, 0.9]$	$0.1172^{+0.0006}_{-0.0009}$
Rp/Rs $_{\mathrm{SOSS1}}$	$\mathcal{U}[0.01, 0.9]$	$0.1197^{+0.0004}_{-0.0004}$
Rp/Rs $_{\mathrm{SOSS2}}$	$\mathcal{U}[0.01, 0.9]$	$0.1204^{+0.0005}_{-0.0005}$
Rp/Rs $_{\mathrm{NRS1}}$	$\mathcal{U}[0.01, 0.9]$	$0.1188^{+0.0002}_{-0.0002}$
Rp/Rs $_{\mathrm{NRS2}}$	$\mathcal{U}[0.01, 0.9]$	$0.1192^{+0.0004}_{-0.0005}$
a/Rs	$\mathcal{U}[1, 25]$	$8.9890^{+0.0222}_{-0.0216}$
b	$\mathcal{U}[0, 1]$	$0.7298^{+0.0020}_{-0.0020}$
$q1_{\mathrm{TESS}}$	$\mathcal{U}[0, 1]$	$0.34^{+0.05}_{-0.05}$
$q2_{\mathrm{TESS}}$	$\mathcal{U}[0, 1]$	$0.14^{+0.10}_{-0.18}$
$q1_{\mathrm{SOSS1}}$	$\mathcal{U}[0, 1]$	$0.14^{+0.01}_{-0.01}$
$q2_{\mathrm{SOSS1}}$	$\mathcal{U}[0, 1]$	$0.46^{+0.13}_{-0.14}$
$q1_{\mathrm{SOSS2}}$	$\mathcal{U}[0, 1]$	$0.29^{+0.02}_{-0.02}$
$q2_{\mathrm{SOSS2}}$	$\mathcal{U}[0, 1]$	$0.58^{+0.10}_{-0.10}$
$q1_{\mathrm{NRS1}}$	$\mathcal{U}[0, 1]$	$0.05^{+0.01}_{-0.01}$
$q2_{\mathrm{NRS1}}$	$\mathcal{U}[0, 1]$	$0.11^{+0.08}_{-0.15}$
$q1_{\mathrm{NRS2}}$	$\mathcal{U}[0, 1]$	$0.04^{+0.01}_{-0.01}$
$q2_{\mathrm{NRS2}}$	$\mathcal{U}[0, 1]$	$0.35^{+0.23}_{-0.29}$

Note. q1 and q2 refer to the D. M. Kipping (2013) reparameterization of the quadratic limb-darkening law. T_0 is fit as the NIRISS midtransit time and also propagated here to the epoch of the NIRSpec transit.

period is unsurprising given that it is primarily constrained by TESS data, which was used in all analyses mentioned above.

2.4. JWST Light Curve Fits

We then fit the spectrophotometric light curves from the JWST datasets, fixing the orbital parameters to those from Table 1. We use the `exoUPRF` package (M. Radica 2024b; E.-M. Ahrer et al. 2025a) for these and fit the light curves for each instrument at three different resolutions: $R=100$, $R=300$, and the native detector resolution ($R\sim3500$ for NIRSpec and $\sim$700 for NIRISS). For each light curve, we fit the scaled planet radius, the transit zero-point, a linear slope, and the additive error inflation term. We experiment with a number of limb-darkening treatments, including varying the parameterization (quadratic, D. M. Kipping 2013 quadratic, four-parameter), as well as the degree of flexibility (freely fitted, fixed, prior) and find negligible differences in the transmission spectra at all wavelengths. We therefore elect to use the quadratic law and put Gaussian priors on the limb-darkening coefficients centered on the values predicted by `ExoTiC-LD` (D. Grant & H. R. Wakeford 2024) using the 3D `stagger` stellar grid (Z. Magic et al. 2015) and widths of 0.2 as recommended by J. A. Patel & N. Espinoza (2022).

The final transmission spectra at $R=300$ are shown in Figure 2 for both instruments. Other comparisons and light curve fitting diagnostics are included in the Zenodo repository. We also perform an additional analysis of both datasets using `NAMELESS` (L.-P. Coulombe et al. 2023, 2025) for NIRISS and `Eureka!` (T. Bell et al. 2022) for NIRSpec. Details of these reductions can be found in Appendix A, and the final $R=300$ spectra are compared to the nominal `exoTEDRF` spectra in Figure 2.

2.4.1. Asymmetric Fits

Finally, we attempt to extract signatures of inhomogeneous morning and evening limbs on WASP-96 b via the transit light curve. We use the `catwoman` (K. Jones & N. Espinoza 2020; N. Espinoza & K. Jones 2021) package for this, which assumes that a transiting planet can be approximated as two conjoined semicircles that can have different radii—thereby allowing for the determination of independent morning and evening limb spectra (P. Von Paris et al. 2016; E. M.-R. Kempton et al. 2018; N. Espinoza & K. Jones 2021).

Again, we fix the orbital parameters to those from Table 1. We then fix the limb-darkening to the quadratic law predictions from `ExoTiC-LD` and include a linear slope as a systematics model. T_0, in particular, is degenerate with the presence of limb asymmetry; however, our sub-10 s precision on T_0 should allow for the extraction of limb asymmetries of a few scale heights (M. M. Murphy et al. 2024a). We fit the light curves at three resolutions: $R=100$, 50, and 25, and the morning and evening limb spectra at R=50 are shown in Figure 3. In Section 5 we conduct a series of tests to quantify the degree to which the morning and evening spectra differ and thus identify the presence, or lack thereof, of limb asymmetry in our observations.

3. Atmosphere Modeling

To interpret the atmospheric spectra of WASP-96 b we use several Bayesian retrieval and forward modeling codes (`POSEIDON`, `NemesisPy`, `PyratBay`, `Aurora`, `ScCHIMERA`). This allows us to ensure that our results are robust to the particularities of a given retrieval code. We also explore the impacts of different retrieval setups (e.g., free versus chemically consistent versus radiative-convective-equilibrium models). We include the optical VLT/FORS2 transmission spectrum from N. Nikolov et al. (2018) in our modeling to extend the wavelength coverage to $\sim$0.35 μm. We also test adding the Magellan/IMACS, and HST/WFC3 spectra, from C. D. McGruder et al. (2022) and N. K. Nikolov et al. (2022), respectively, but find their impacts to be negligible. This is due to these spectra providing redundant wavelength coverage at lower precision than VLT/FORS2 and NIRISS/SOSS, respectively.

The base setup for each modeling code is described in the following sections. An example corner plot from the `POSEIDON` free retrieval on the nominal VLT + $R=300$ JWST NIRISS and NIRSpec data combination is included in Appendix D and corner plots from other relevant runs are included in the associated Zenodo repository.

3.1. `POSEIDON`

The first code that we use is the open-source `POSEIDON` package (R. J. MacDonald & N. Madhusudhan 2017; R. J. MacDonald 2023). We run free retrievals, where each absorber can vary independently and has a constant abundance with altitude. We include opacity from H_2O, CO_2, CO, CH_4, H_2S, SO_2, Na, K, HCN, and NH_3 (all references included in Table 4), as well as H_2-H_2 and H_2-He collision-induced absorption (CIA). We include contributions of aerosols via a cloud-haze prescription, using a gray slab cloud at pressure P_{cloud} and a modified Rayleigh scattering slope, with an enhancement factor α and scattering slope γ, where $\gamma=-4$ represents H_2 Rayleigh scattering (e.g., R. J. MacDonald &

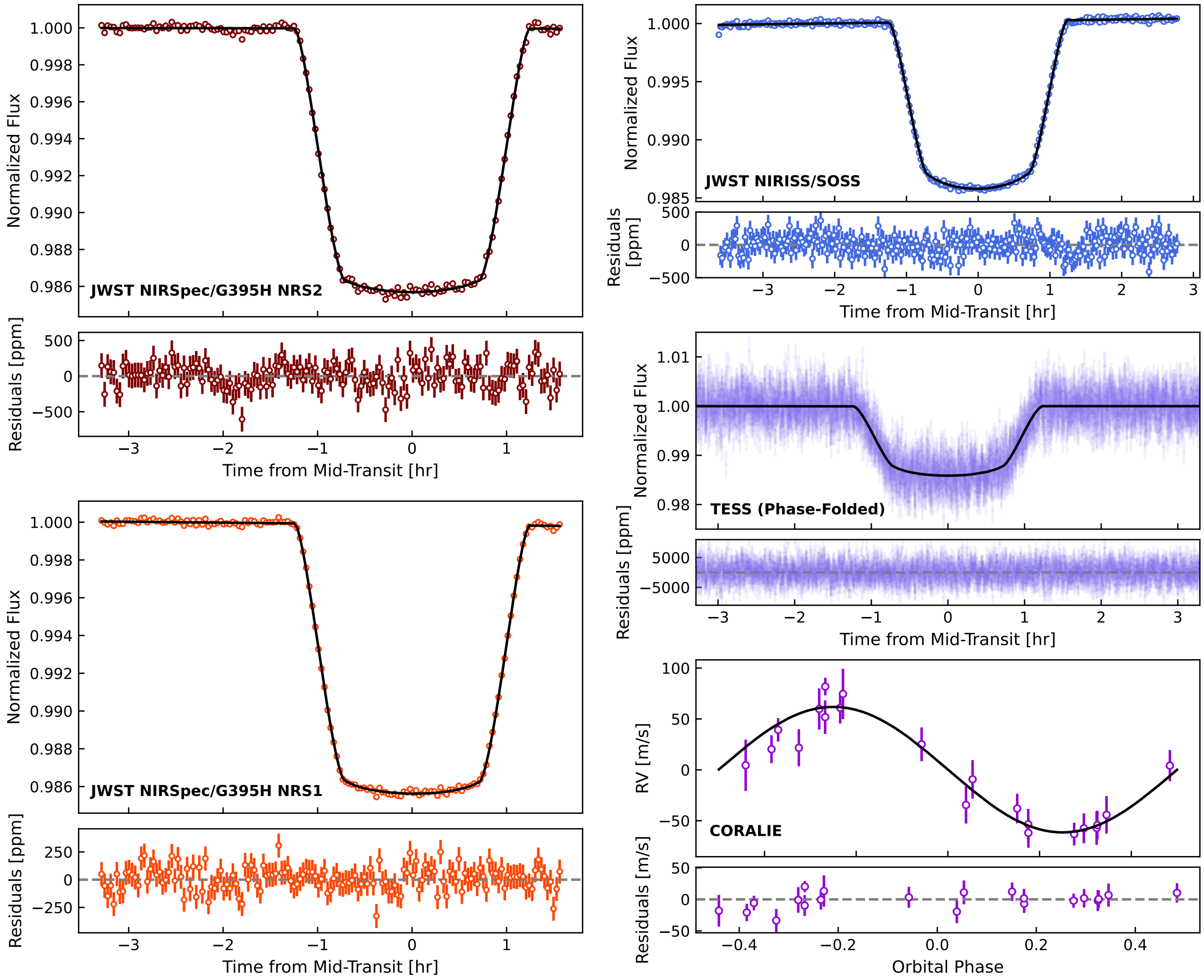

Figure 1. Data (colored points) and best-fitting models (black) from the joint transit and RV fit. Residuals to the best-fitting model are shown below each dataset. The TESS and CORALIE data have been phase folded to the best-fitting orbital period.

N. Madhusudhan 2017; A. Pinhas et al. 2018). We also allow for inhomogeneous “patchy” aerosols via the prescription of M. R. Line & V. Parmentier (2016).

We generate an isothermal, plane-parallel atmosphere model spanning 2 to −7 bar in log pressure at a resolution of $R = 20{,}000$, which has been demonstrated to be sufficient for JWST transmission spectra of giant planets (e.g., D. R. Louie et al. 2025). We include offsets between each dataset (relative to NIRISS) when jointly retrieved on, and sample the posterior space using the `MultiNest` sampling algorithm (F. Feroz et al. 2009) with 1000 live points.

3.2. *PyratBay*

We also used the `PyratBay` framework (P. E. Cubillos & J. Blecic 2021) to model the atmosphere of WASP-96 b. `PyratBay` is a comprehensive spectrum synthesis and atmospheric retrieval tool designed for exoplanet studies. For this analysis, we employed a free-chemistry retrieval framework and generated models incorporating the NIRISS and NIRSpec observations, with and without ground-based data from VLT/FORS2. We further examined how different data resolutions affect the retrieved atmospheric properties and overall conclusions.

We include opacity from H_2O, Na, K, CH_4, NH_3, HCN, CO, CO_2, and SO_2 (summarized in Table 4). In addition, we incorporated the Rayleigh scattering from A. Lecavelier Des Etangs et al. (2008), which includes the strength (f_{ray}) and power-law index (α_{ray}) of the scattering opacity cross-section, and a gray cloud deck where the atmosphere becomes instantly opaque at all wavelengths at a requested pressure level. Inhomogeneous clouds were incorporated following M. R. Line & V. Parmentier (2016). We also adopt the parametric temperature–pressure profile of N. Madhusudhan & S. Seager (2009).

The set of free parameters included the abundances of the nine aforementioned chemical species assuming uniform priors, six parameters describing the temperature–pressure profile, one parameter for the planetary radius at a reference pressure of 0.1 bar, two parameters for Rayleigh scattering, one parameter for the cloud-top pressure of a gray cloud model, and one parameter describing cloud patchiness (f_{patchy}). The parameter space was explored using the Nested Sampling algorithm implemented in `PyMultiNest` (J. Skilling 2006; J. Buchner et al. 2014), with 2000 live points in all retrievals.

3.3. *NemesisPy*

`NEMESIS` is a radiative transfer and retrieval tool originally developed to study planetary atmospheres within the solar system (P. G. J. Irwin et al. 2008), but extensively adapted to study exoplanet atmospheres (e.g., J. K. Barstow et al. 2017;

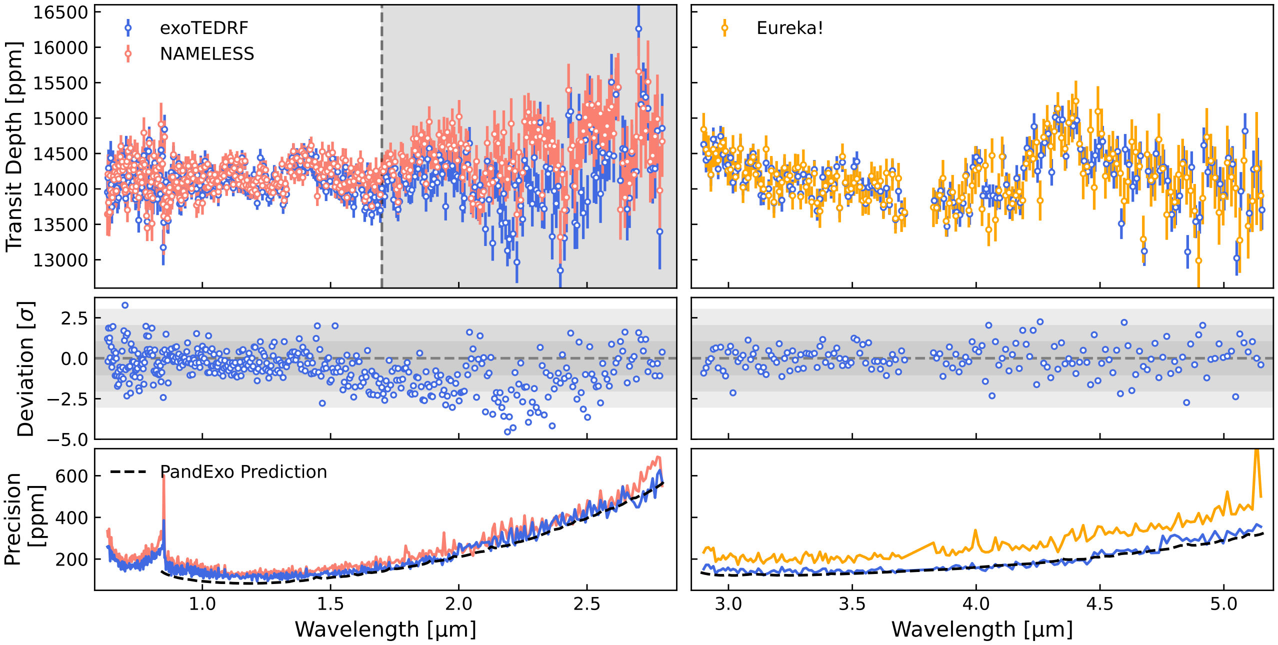

Figure 2. Comparison between our nominal `exoTEDRF` spectra and alternate reductions with `NAMELESS` for NIRISS (left panels) and `Eureka!` for NIRSpec (right panels). Top: the two spectra produced for each instrument overplotted. The gray shading in the NIRISS panel denotes wavelengths not used in the comparative retrievals (see Section 3). Middle: error-normalized differences for each instrument. There is a significant divergence between the two NIRISS/SOSS spectra redwards of ∼1.7 μm, which can be attributed to differences in $1/f$ noise correction methodologies (see Appendix B). Bottom: light curve scatter as a function of wavelength compared to `PandExo` predictions.

J. Taylor & V. Parmentier 2023). The framework is now fully pythonized, and we use this version of the code for this analysis (called `NemesisPy` from here on out; J. Yang et al. 2024). `NemesisPy` uses the correlated-k method to compute the molecular and atomic opacities (A. A. Lacis & V. Oinas 1991) and nested sampling, specifically `PyMultiNest` to sample the parameter space (J. Skilling 2006; J. Buchner et al. 2014). Included opacity sources are the same as above and summarized in Table 4. Gas opacities are computed using k-tables with resolution $R = 1000$, obtained from the ExoMol database (K. L. Chubb et al. 2021), before being channel averaged to the resolution of the observations. We perform both a free chemistry and chemical equilibrium retrieval in which we utilize `FastChem` (J. W. Stock et al. 2022) to obtain values for the atmospheric metallicity and C/O.

We model clouds/hazes following the prescription derived in R. J. MacDonald & N. Madhusudhan (2017), where we fit for a cloud-top pressure, a Rayleigh enhancement factor, a scattering slope, and a cloud fraction. As is typical when combining observations from different instruments, we anchor our retrieval to the NIRISS/SOSS observations and fit for offsets for VLT, Magellan, and NIRSpec NRS1 and NRS2. The priors used for all parameters are listed in Table 2. We sample the parameter space using 1000 live points and have an evidence tolerance of 0.5.

3.4. `Aurora`

The final retrieval framework that we use is `Aurora` (L. Welbanks & N. Madhusudhan 2021). `Aurora` assumes a one-dimensional plane-parallel atmosphere and solves the requisite radiative transfer equations for hydrostatic equilibrium to produce a transmission spectrum of the planet.

As with the other retrieval frameworks, we model the temperature–pressure profile using the six-parameter prescription of N. Madhusudhan & S. Seager (2009). We use the two sector cloud and haze prescription from L. Welbanks & N. Madhusudhan (2021) where the hazes are parameterized as a deviation from H_2-Rayleigh scattering (A. Lecavelier Des Etangs et al. 2008) and clouds are parameterized through a gray cloud deck at a given pressure layer. The clear and cloudy/hazy atmospheric models are combined following M. R. Line & V. Parmentier (2016).

Our atmospheric models consider opacity from the same set of species as the other codes (summarized in Table 4) and fit for offsets between instruments and detectors, as has been previously done for panchromatic JWST spectra (e.g., A. L. Carter et al. 2024). We apply a nested sampling approach for our retrievals, using the MultiNest sampler (F. Feroz et al. 2009) via the PyMultiNest python wrapper (J. Buchner et al. 2014), with 1000 live points used for sampling.

3.5. `ScCHIMERA`

We further consider atmospheric models under the assumption of radiative-convective-thermo/photochemical equilibrium. These models are generated using `ScCHIMERA` (T. J. Bell et al. 2023; L. Welbanks et al. 2024; L. S. Wiser et al. 2025) calculating the vertical temperature structure and chemical composition of the planet's atmosphere for a given heat redistribution, atmospheric metallicity, and C/O ratio. ScCHIMERA solves the radiative transfer between layers utilizing the two-stream approximation (O. B. Toon et al. 1989) and absorbers expected in exoplanet atmospheres under the assumption of thermochemical equilibrium; these are calculated using the `CEA2` module (S. Gordon & B. J. Mcbride 1994), which, for each layer, minimizes the Gibbs free

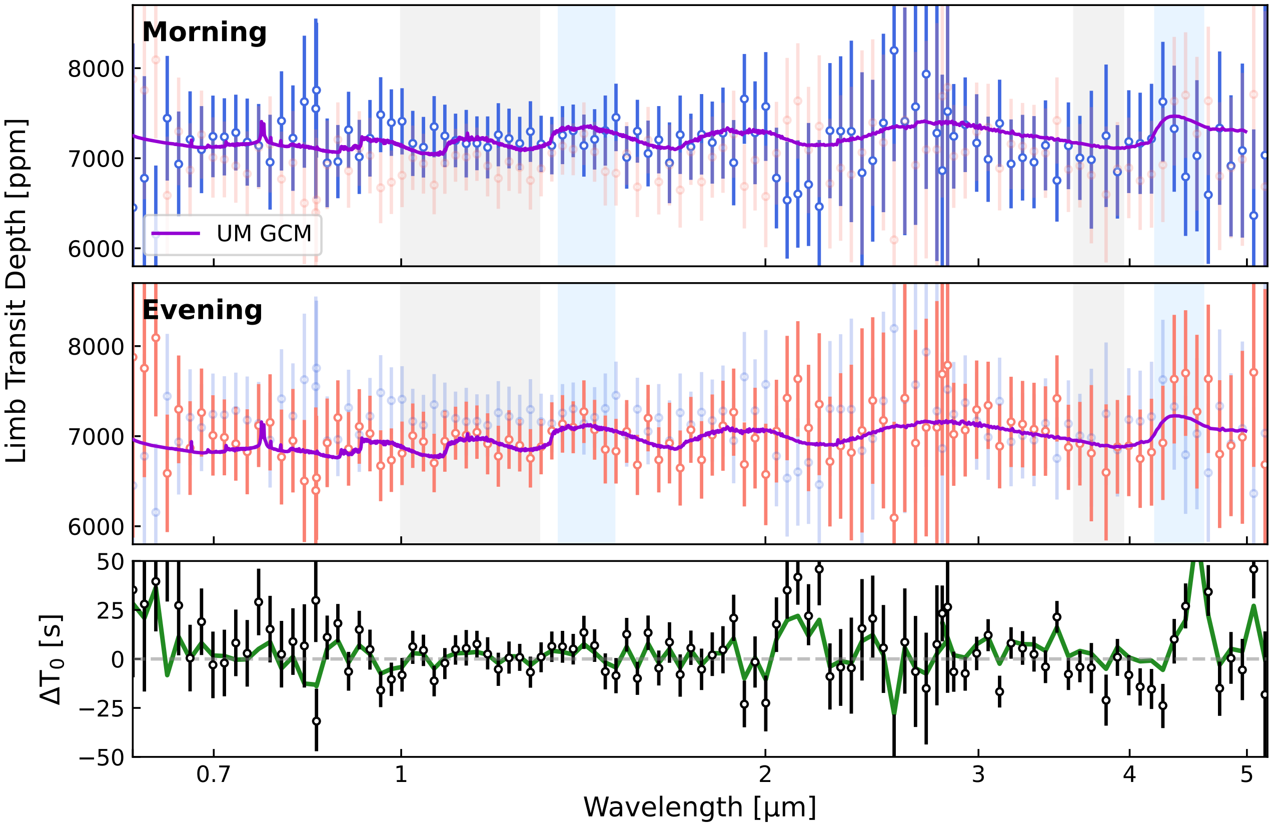

Figure 3. WASP-96 b's morning and evening limb transmission spectra as observed with JWST. Top: the morning-limb transmission spectrum (blue data points) compared to the evening limb spectrum (faded red). Overplotted in purple is the morning-limb spectrum from the aerosol-free, 10× solar UM GCM run (see Appendix C). Blue and gray shaded rectangles denote the in-band and out-of-band wavelengths, respectively, for the H_2O and CO_2 band amplitude calculations (see Section 5.1). Middle: inverse of the above, focusing on the evening limb spectrum. Bottom: fitting midtransit time as a function of wavelength assuming a uniform-limb (i.e., `batman`) planet (black points). In green is the T_0 spectrum derived from the asymmetric `catwoman` fits using the formalism of M. M. Murphy et al. (2024a).

energy and provides chemical abundances. A description of the thermochemical data sources is provided in B. J. Mcbride et al. (1993), with the iteration done using a Newton–Raphson scheme (C. P. McKay et al. 1989). Then, we solve for chemical kinetics in the atmosphere given an incident stellar flux to account for the effects from chemical disequilibrium (e.g., photochemistry) using `Photochem` (N. F. Wogan et al. 2025). Our grid of models follows the same spacing and dimensions as that used in M. Radica et al. (2023) with the exception of metallicity, which in this work has log-metallicities between −1.0 and 1.625 in spacing of 0.125 dex. We adopt solar abundances from K. Lodders et al. (2009).

We use this grid of models to fit the transmission of WASP-96 b using `CHIMERA` (M. R. Line et al. 2013) considering absorption due to H_2O, CO, CO_2, CH_4, NH_3, H_2S, HCN, C_2H_2, Na, K, and SO_2 as well as H_2-H_2 and H_2-He CIA (references in Table 4). We include the presence of inhomogeneous clouds/hazes following the same description as in Aurora above. In total, we fit for 12 parameters: redistribution factor f, atmospheric metallicity Z, C/O, radius scaling $\times R_p$, cloud opacity κ, Rayleigh scattering amplitude a, haze slope γ, cloud/haze covering fraction $\phi_{\rm cloud\ and\ hazes}$, and offsets for all instruments relative to NIRISS. Parameter estimation is performed using MultiNest (F. Feroz et al. 2009) via the PyMultinest wrapper (J. Buchner et al. 2014).

4. Optical-to-IR Atmosphere Characterization of WASP-96 b

4.1. Overview of Model Results

Table 2 presents the results from the full gamut of retrieval tests run on the transmission spectra of WASP-96 b. We take as our nominal results the inferences from the full $R = 300$ JWST + VLT combination. We also run a resolution test using `Pyrat Bay` varying the resolution of the JWST data, and another test with `NemesisPy` including the Magellan and HST data in the analysis, neither of which significantly affects the results. The best-fitting models from each retrieval code on the nominal data configuration are shown in Figure 4. We also include, in the figure and not the retrievals, the 3.6 and 4.5 μm Spitzer/IRAC transit depths from N. K. Nikolov et al. (2022) for comparison. Although the 4.5 μm point agrees well with the new JWST NIRSpec data, the 3.6 μm point does not—making this one of the few times that JWST data have contradicted previous observations from Spitzer.

There are significant differences between the NIRISS spectra from `exoTEDRF` and `NAMELESS` at wavelengths $\gtrsim$2 μm (Figure 2), which we show in Appendix B is due to the $1/f$-noise correction method and argue that the group-level correction used in `exoTEDRF` is more correct. However, we verify that our atmosphere inferences still hold when retrieving on the `NAMELESS` + `Eureka!` spectrum when removing this discrepant region.

Table 2

Retrieved Atmosphere Constraints for WASP-96 b

Parameter	Prior Range	`POSEIDON`		`NemesisPy`			`Pyrat Bay`				`Aurora`	`ScCHIMERA`
		Free[a]	Alt. Free[b]	Free[a]	Alt. Free[c]	Chem. Equi.[a]	Free[a]	$R = 100$[d]	$R = 300$[d]	pixel[d]	Free	Grid
T [K][e]	$\mathcal{U}[200, 2000]$	1093^{+54}_{-49}	1044^{+131}_{-79}	1017^{+79}_{-72}	1085^{+66}_{-64}	961^{+46}_{-37}	1029^{+94}_{-82}	977^{+96}_{-84}	1036^{+215}_{-119}	949^{+102}_{-106}	939^{+25}_{-27}	—
log H_2O	$\mathcal{U}[-12, -1]$	$-2.61^{+0.27}_{-0.30}$	$-2.82^{+0.62}_{-0.76}$	$-2.82^{+0.24}_{-0.26}$	$-2.79^{+0.25}_{-0.26}$	—	$-2.67^{+0.29}_{-0.28}$	$-2.30^{+0.38}_{-0.41}$	$-2.36^{+0.32}_{-0.38}$	$-2.63^{+0.28}_{-0.26}$	$-2.76^{+0.30}_{-0.28}$	—
log CH_4	$\mathcal{U}[-12, -1]$	<-5.91	<-5.35	<-5.81	<-5.88	—	$-5.75^{+0.27}_{-0.26}$	$-6.58^{+0.72}_{-2.73}$	$-5.87^{+0.35}_{-0.42}$	$-5.93^{+0.26}_{-0.26}$	<-6.18	—
log CO_2	$\mathcal{U}[-12, -1]$	$-4.65^{+0.34}_{-0.39}$	$-4.15^{+0.70}_{-0.77}$	$-4.91^{+0.30}_{-0.30}$	$-4.88^{+0.31}_{-0.31}$	—	$-4.48^{+0.32}_{-0.30}$	$-4.49^{+0.42}_{-0.43}$	$-4.34^{+0.35}_{-0.38}$	$-4.50^{+0.31}_{-0.30}$	$-4.46^{+0.34}_{-0.31}$	—
log CO	$\mathcal{U}[-12, -1]$	<-2.92	<-2.23	<-4.36	<-4.41	—	<-4.13	<-3.85	<-4.23	<-3.17	<-2.96	-
log SO_2	$\mathcal{U}[-12, -1]$	$-5.67^{+0.31}_{-0.32}$	$-5.63^{+0.60}_{-0.59}$	$-6.01^{+0.30}_{-0.39}$	$-6.02^{+0.31}_{-0.41}$	—	$-5.47^{+0.29}_{-0.28}$	$-6.63^{+0.94}_{-3.09}$	$-5.51^{+0.32}_{-0.35}$	$-6.35^{+0.38}_{-1.01}$	$-5.52^{+0.29}_{-0.28}$	—
log H_2S	$\mathcal{U}[-12, -1]$	<-3.99	<-3.49	<-4.18	<-4.21	—	—	—	—	—	—	—
log Na	$\mathcal{U}[-12, -1]$	$-4.10^{+0.47}_{-0.52}$	$-4.29^{+1.00}_{-1.29}$	$-3.59^{+0.47}_{-0.55}$	$-3.53^{+0.45}_{-0.48}$	—	$-3.99^{+0.64}_{-0.81}$	<-2.18	<-2.37	<-3.16	$-4.15^{+0.63}_{-0.76}$	—
log$K$	$\mathcal{U}[-12, -1]$	<-5.45	<-4.57	<-5.01	<-5.12	—	<-4.89	<-3.68	<-4.00	<-5.35	<-4.92	—
log NH_3	$\mathcal{U}[-12, -1]$	<-5.47	<-3.91	<-5.87	<-5.89	—	<-5.67	<-4.97	<-5.49	<-5.46	<-5.49	—
log HCN	$\mathcal{U}[-12, -1]$	<-4.64	<-3.68	<-5.48	<-5.46	—	<-4.41	<-4.59	<-5.05	$-5.67^{+0.34}_{-0.36}$	<-4.67	—
log $P_{\rm cloud}$ [bar]	$\mathcal{U}[-6, 2]$	>-1.91	>-2.92	>-1.86	>-1.77	>-2.36	>-2.07	>-2.71	>-2.14	>-1.49	>-1.90	—
$f_{\rm Ray}$[e]	$\mathcal{U}[0, 10]$	$1.51^{+0.34}_{-0.31}$	$0.58^{+0.74}_{-0.69}$	$1.80^{+0.27}_{-0.27}$	$2.67^{+0.23}_{-0.22}$	$2.46^{+0.34}_{-0.32}$	$1.15^{+0.26}_{-0.24}$	$2.03^{+0.43}_{-0.40}$	$2.04^{+0.36}_{-0.37}$	$1.57^{+0.28}_{-0.25}$	$1.31^{+0.34}_{-0.28}$	$2.88^{+0.60}_{-0.53}$
$\alpha_{\rm Ray}$[e]	$\mathcal{U}[-5, 5]$	$-2.28^{+0.36}_{-0.41}$	$-2.29^{+0.71}_{-0.72}$	$-2.11^{+0.32}_{-0.31}$	$-1.97^{+0.31}_{-0.28}$	$-3.36^{+0.18}_{-0.18}$	$-1.51^{+0.23}_{-0.24}$	$-2.34^{+0.38}_{-0.44}$	$-2.64^{+0.39}_{-0.47}$	$-2.96^{+0.34}_{-0.37}$	$-1.89^{+0.29}_{-0.32}$	$-3.22^{+0.77}_{-0.64}$
[M/H]	$\mathcal{U}[-2, 3]$	—	—	—	—	$1.14^{+0.15}_{-0.15}$	—	—	—	—	—	$0.81^{+0.13}_{-0.15}$
C/O	$\mathcal{U}[0, 1.5]$	—	—	—	—	$0.25^{+0.13}_{-0.09}$	—	—	—	—	—	$0.44^{+0.10}_{-0.09}$

Notes. Results reported as median and 1σ range for bounded posteriors and 3σ limits otherwise. "—" indicates that a parameter was not included in a retrieval.

[a] Retrievals performed on combined VLT + `exoTEDRF` JWST spectrum, with JWST data binned to $R = 300$.

[b] Same as *a*, but using the alternate `NAMELESS` NIRISS and `Eureka!` NIRSpec JWST spectra.

[c] Same as *a*, but including Magellan/IMACS and HST/WFC3 data.

[d] Retrievals performed on `exoTEDRF` JWST data only.

[e] Isothermal atmosphere temperature for `POSEIDON`, and top-of-atmosphere temperature for `NemesisPy`, `Pyrat Bay`, and `Aurora`, following the PT parameterization of N. Madhusudhan & S. Seager (2009).

[f] $f_{\rm Ray}$ is the Rayleigh enhancement factor and $\alpha_{\rm Ray}$ the scattering slope for "haze scattering" opacity.

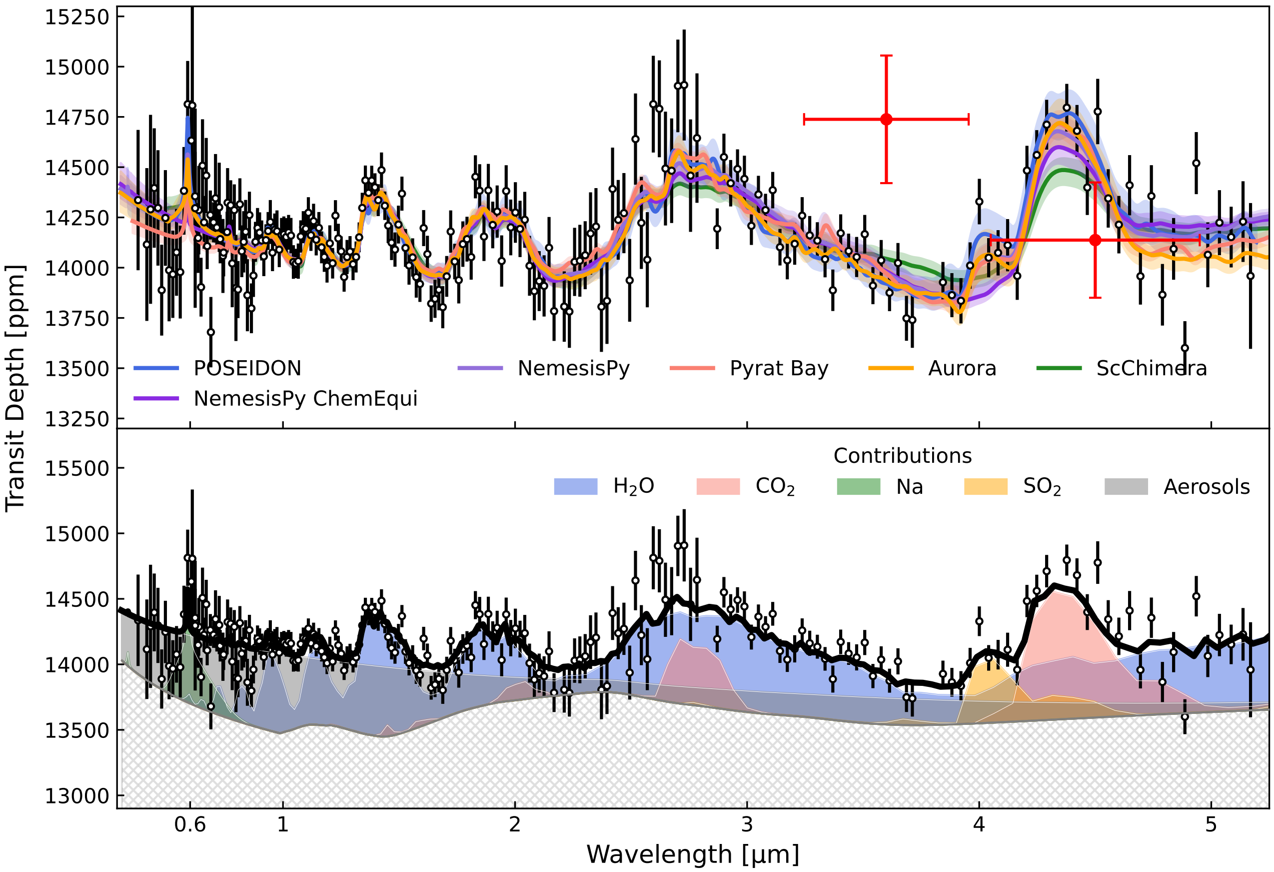

Figure 4. Results of modeling WASP-96 b's transmission spectrum. Top: best-fitting atmosphere models from each retrieval code (colored lines) along with the 2σ confidence envelopes (colored shading) overplotted on the combined ground-based + JWST spectrum (black data points). The JWST data have been binned from the nominal resolution of $R = 300$ to $R \sim 100$ for plotting purposes. Also shown in red, but not included in the retrievals, are the Spitzer 3.6 and 4.5 μm transit depths from N. K. Nikolov et al. (2022). The 3.6 μm point in particular, is discrepant with the NIRSpec observations. Bottom: spectral decomposition of the transmission spectrum to show contributions from various chemical species as well as aerosols (here primarily a scattering slope).

In the following sections, we highlight some key findings and their implications for the atmosphere of WASP-96 b. Where comparisons with stellar values are made, stellar abundances are sourced from N. K. Nikolov et al. (2022). We also use M. Asplund et al. (2009) as the reference for solar values to remain consistent with N. K. Nikolov et al. (2022).

4.2. Atmospheric Composition of WASP-96 b

Particularly with the addition of our new NIRSpec/G395H data, we reveal a rich transmission spectrum for WASP-96 b. In Figure 5, we compare the retrieved abundances of several key species from the POSEIDON and Aurora free retrievals to predictions from chemical equilibrium and findings from the ScCHIMERA self-consistent grid. Prominent H_2O and CO_2 features are visible and we retrieve abundances spanning log VMR $-2.82^{+0.62}_{-0.76}$ to $-2.30^{+0.38}_{-0.41}$ and $-4.91^{+0.30}_{-0.30}$ to $-4.15^{+0.70}_{-0.77}$, respectively, depending on the data and retrieval setup. The H_2O abundance is consistent with the findings of N. K. Nikolov et al. (2022) and L.-C. Wang et al. (2026), but slightly higher than that of J. Taylor et al. (2023).

Na is also clearly visible in the spectrum though its abundance is only constrainable with the contributions of the VLT data—JWST observations alone yield an upper limit (e.g., J. Taylor et al. 2023). There is more variance in the retrieved Na abundance compared to other species, with values ranging from log VMR $-4.29^{+1.00}_{-1.29}$ to $-3.53^{+0.45}_{-0.48}$ depending on

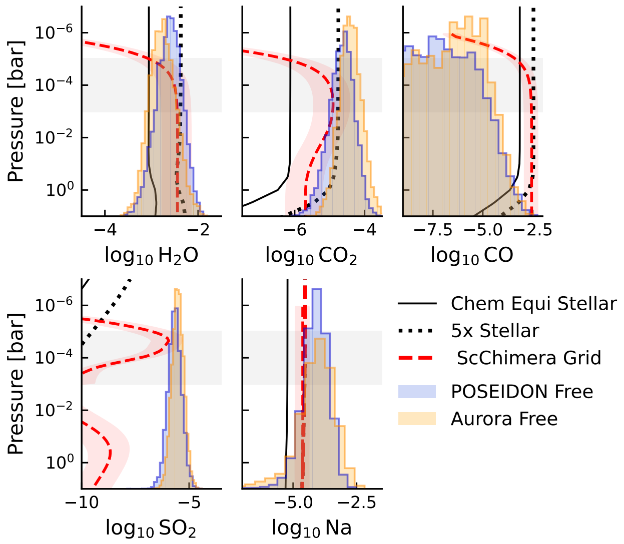

Figure 5. Abundances of several prominent chemical species inferred from the POSEIDON (blue histograms) and Aurora (orange histograms) free retrievals. Overplotted are chemical equilibrium abundance profiles for a stellar (log$Z$~2× solar, C/O=0.42; solid) and 5× stellar (log$Z$~10× solar; dotted) metallicity atmosphere, as well as constraints from the self-consistent grid (red). The gray shaded regions denote the approximate pressures probed by these observations. Solar abundances are taken to be those from M. Asplund et al. (2009) to match N. K. Nikolov et al. (2022).

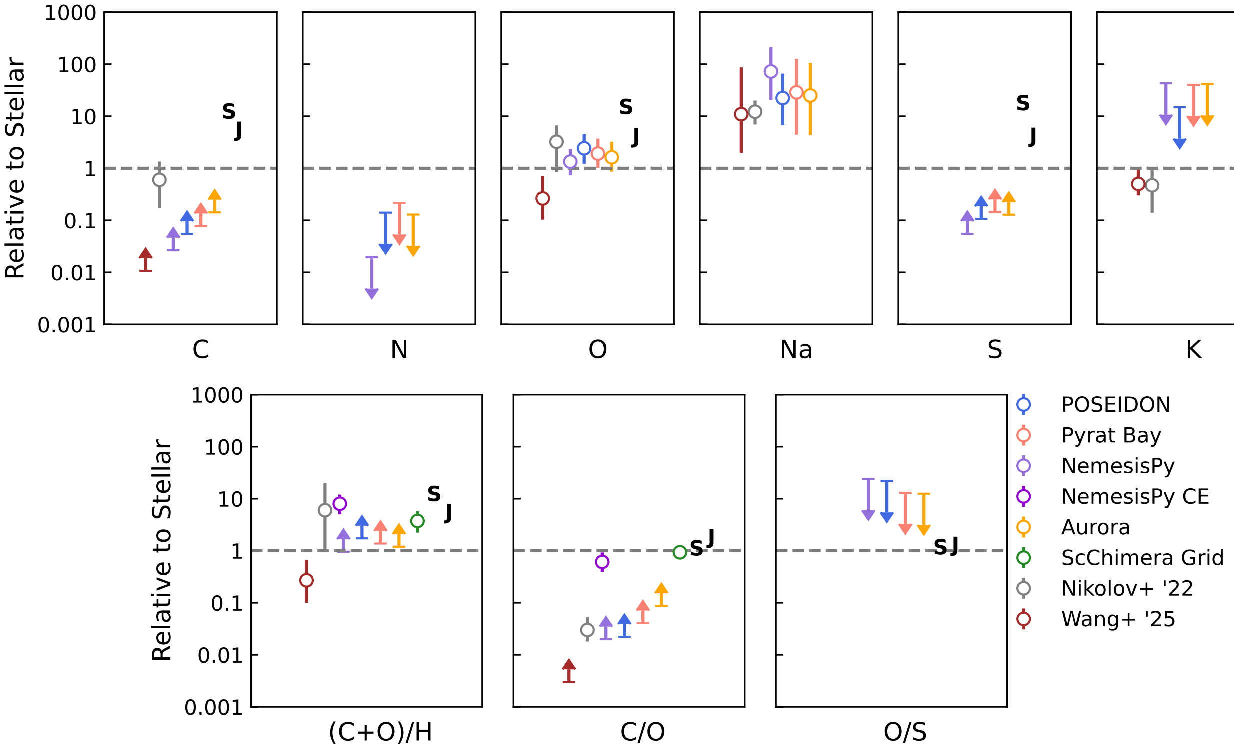

Figure 6. Elemental abundances and ratios in the atmosphere of WASP-96 b. Top row: derived elemental abundances for WASP-96 b's atmosphere from each retrieval code (colored points) normalized to stellar values (N. K. Nikolov et al. 2022). For bounded constraints, the posterior median and 1σ confidence interval are shown. Otherwise, 3σ upper limits are plotted. The approximate locations of Jupiter and Saturn (sourced from S. K. Atreya et al. 2022) are marked with bold letters. Bottom row: abundance ratios derived from the above elemental constraints.

the data and retrieval setup. These constraints are consistent with L.-C. Wang et al. (2026) and slightly more elevated than those found by N. K. Nikolov et al. (2022), though still consistent at $\lesssim 2\sigma$ in all cases.

We find moderate evidence for the presence of SO_2 with abundances ranging from log VMR $-6.01^{+0.30}_{-0.39}$ to $-5.47^{+0.29}_{-0.28}$ across the different retrievals. We discount the `Pyrat Bay` $R = 100$ retrieval here since the SO_2 feature is not fully resolved at this resolution and its abundance is not well constrained. To quantify the model preference for the inclusion of SO_2, we ran an additional `NemesisPy` retrieval using the nominal setup but leaving out SO_2. We find an evidence value of $\ln Z = -596.57$ compared to -593.88 for the nominal setup, yielding a Bayes factor of $\ln B = 2.69$—or moderate evidence for SO_2 using the Jeffreys scale (H. Jeffreys 1935).

As shown in Figure 5 the `ScCHIMERA` + `Photochem` SO_2 abundance is well-matched to the values from the free retrievals at the pressure levels probed by our observations. Based on its equilibrium temperature and atmospheric metallicity, WASP-96 b falls directly on the SO_2 shoreline derived by I. J. M. Crossfield et al. (2025), and our retrieved SO_2 abundance agrees with their grid, assuming a 10–20× solar atmosphere metal enrichment. If confirmed via follow-up observations (e.g., MIRI/LRS) this finding would validate the I. J. M. Crossfield et al. (2025) shoreline in a higher-temperature regime ($T_{\rm eq} \sim 1300$ K compared to, e.g., ~ 1100 K for WASP-39 b).

On the other hand, we do not find any evidence for the presence of CO, which should be a major carrier of both O and C at these temperatures (J. I. Moses et al. 2011; N. Madhusudhan 2012). Our inability to place a bounded constraint on CO is likely driven by a combination of insufficient precision redwards of 4.5 μm where CO is most visible and the presence of a strong CO_2 feature at 4.3 μm, which can hide part of the CO absorption band in transmission spectra. Indeed, with the exception of WASP-107 b and WASP-39 b, other planets with robust CO detections in transit have had weak or nonexistent CO_2 features (E.-M. Ahrer et al. 2025a; J. Kirk et al. 2025; A. Meech et al. 2025). WASP-107 b, though, is a superpuff with massive atmosphere features, which allows the easy identification of molecular features (e.g., L. Welbanks et al. 2024), and in WASP-39 b CO was identified through a cross-correlation analysis instead of the standard retrieval approach.

In general, with the exception of CO our freely retrieved abundances agree well with chemical equilibrium predictions and the results from the self-consistent grid (Figure 5). Additionally, Figure 6 summarizes our findings for both elemental abundances and ratios, normalized to stellar values (from N. K. Nikolov et al. 2022). Taken together, the freely retrieved H_2O and CO_2 abundances indicate metallicity (as C+O/H) lower limits ranging from 1 to 4× stellar or 2–8× solar, depending on the particular retrieval code. The lack of constraint on the abundance of CO, which should be a prominent carrier of C in particular, prevent a bounded metallicity constraint from free retrievals alone. However, with CO self-consistently included, the `ScCHIMERA` grid finds a metallicity of 2–6× stellar (4–12× solar). The `NemesisPy` chemical equilibrium retrievals yield an even higher metallicity of 5–12× stellar (∼10–20× solar), though, of all models it provides the worst fit to the spectrum, not capturing the SO_2 feature in particular. This is due to `FastChem` only considering thermochemical equilibrium processes, whereas SO_2 is photochemically produced—further underlining the importance of photochemistry in WASP-96 b's atmosphere. In general, though, all models indicate a solar-to-supersolar metallicity atmosphere heavily influenced by photochemistry. These results also highlight the importance of considering multiple modeling schemes with varying amounts of flexibility, since critical abundances and ratios can be difficult to measure with free retrievals alone.

We obtain bounded constraints on CH_4 only in our `Pyrat Bay` retrievals (which use different, higher-resolution opacities; see Section 3.2 and Table 4), at abundances far above chemical equilibrium expectations for the upper atmosphere. As demonstrated by M. Zamyatina et al. (2024), due to longitudinal quenching, CH_4 could be present in detectable abundances in WASP-96 b's terminator atmosphere at lower metallicities (1× solar), but not at higher values (10× solar). Moreover, strong vertical mixing could also cause CH_4 to quench in the deep atmosphere where its abundance is more comparable to the values found by `Pyrat Bay`. However, even if substantial quantities of CH_4 are transported to the terminator upper atmosphere, it is unlikely that they would be able to persist due to the susceptibility of CH_4 to photodissociation (B. Fleury et al. 2023). Finally, the retrievals also do not reveal evidence for H_2S, K, HCN, or NH_3.

Our inferred composition is in broad agreement with previous studies of the atmosphere of WASP-96 b (e.g., K. H. Yip et al. 2021; C. D. McGruder et al. 2022; N. K. Nikolov et al. 2022). As shown in Figure 6, our O and Na abundances are consistent with N. K. Nikolov et al. (2022). However, we do not find evidence for K whereas N. K. Nikolov et al. (2022) do. Though, we are able to place more robust constraints on the atmosphere metallicity as the presence of CO_2 implies values above solar. On the other hand, our results are in tension with the findings of L.-C. Wang et al. (2026), particularly their inference of a substellar metallicity, which is incompatible with our robust detection of CO_2. This highlights the need to simultaneously analyze multiple chemical species to place robust constraints on atmosphere metallicity.

4.2.1. Implications for Planet Formation

Planet atmospheres are predicted to retain clues into the planet's formation and migration history (K. I. Öberg et al. 2011; C. Mordasini et al. 2016; Y. Chachan et al. 2023; I. J. M. Crossfield 2023; J. Kirk et al. 2025). Elemental ratios, in particular, are key in this endeavor (e.g., K. I. Öberg et al. 2011; Y. Chachan et al. 2023) and since we have evidence for O-, C-, and S-bearing species, we can begin to construct multiple such ratios. The composition of WASP-96 itself is also well characterized (N. K. Nikolov et al. 2022) meaning we can compare elemental ratios derived from the atmosphere of WASP-96 b to that of the host stars, which are widely used as representative of the protostellar environment.

As shown in the lower panels of Figure 6, the free retrievals yield a lower limit on the C/O ratio—enormously influenced by the nondetection of CO, which should be the dominant carried of C in WASP-96 b's atmosphere. With the inclusion of additional physics constraints, the chemical equilibrium and self-consistent grid models obtain bounded constraints of $0.25^{+0.13}_{-0.09}$ and $0.44^{+0.10}_{-0.09}$ respectively—substellar-to-stellar given the C/O ratio of WASP-96 is 0.42 (N. K. Nikolov et al. 2022).

WASP-96 b's broadly superstellar metallicity and stellar-to-superstellar alkali abundances matches the results from L. Welbanks et al. (2019). Considering the substellar-to-stellar derived C/O ratios, our result joins similar findings for giant transiting planets (e.g., E.-M. Ahrer et al. 2023; J. Kirk et al. 2025; A. Meech et al. 2025). In combination, these two factors generally indicate formation beyond the H_2O snowline, followed by disk-driven migration and the accretion of O-rich solid material, which can elevate the planet's metallicity and lower its C/O ratio (M. Ali-Dib 2017; N. Espinoza et al. 2017; A. J. Cridland et al. 2019; A. B. T. Penzlin et al. 2024).

Recent theoretical work has demonstrated that moving beyond the standard metallicity versus C/O prescriptions and considering, e.g., refractory-to-volatile ratios can break degeneracies in planet formation scenarios (e.g., J. D. Lothringer et al. 2021; Y. Chachan et al. 2023; I. J. M. Crossfield 2023). In particular, I. J. M. Crossfield (2023) suggested using the S abundance as a tracer of a planet's refractory content, thereby allowing for the construction of refractory-to-volatile ratios with NIR spectra alone. However, without a constraint on the abundance of H_2S, which should be the dominant S carrier at the temperatures of WASP-96 b's atmosphere (S.-M. Tsai et al. 2023), we can only derive a relatively unconstraining O/S ratio, compatible with multiple formation scenarios. This highlights the importance of H_2S to the goal of understanding S chemistry in exoplanet atmospheres. Unfortunately, the main NIR absorption feature from H_2S at $\sim 3.9\,\mu m$ falls in the NIRSpec/G395H detector gap. Future observations should consider using the G395M grating (or PRISM if possible), which does not have a detector gap, if a primary goal is to constrain a planet's S inventory.

4.3. Aerosols After All?

Across all model tests and data combinations we find that aerosol-free models cannot adequately fit the data. When using the cloud-haze parameterization the opaque cloud deck is generally placed below the observable photosphere, but a scattering slope is consistently inferred. If due to aerosols, sloped opacity requires the presence of small particles (H. R. Wakeford & D. K. Sing 2015), irrespective of whether they are photochemically produced (i.e., hazes) or condensates (i.e., clouds). Both sources are possible a priori, with the temperature of WASP-96 b being ideal for cloud formation (e.g., D. Samra et al. 2023; Figure 7) and the presence of SO_2 indicating the effectiveness of photochemistry on WASP-96 b.

Our results stand in contrast to most previous observational studies of WASP-96 b, which have not seen the same optical slope as we do here (e.g., N. Nikolov et al. 2018; K. H. Yip et al. 2021; C. D. McGruder et al. 2022; N. K. Nikolov et al. 2022). These previous analyses, though, required offsets between ground-based and HST spectra, which without overlapping wavelength coverage can be difficult to constrain (K. H. Yip et al. 2021; C. D. McGruder et al. 2022; N. K. Nikolov et al. 2022). As demonstrated by M. Radica et al. (2023), an offset between the VLT and HST spectrum could mask the slope seen here.

We are though, in line with the findings of M. Radica et al. (2023) and J. Taylor et al. (2023) who analyzed only the JWST NIRISS data. Those studies also highlight the additional degeneracy between the abundance of Na and the presence of a scattering slope, particularly since NIRISS only covers the red wing of the Na feature. Due to our addition of ground-based optical data, which fully resolves the Na feature, this degeneracy is more mitigated. However, we cannot fully discount the possibility that the slope is caused by broad Na wings and that our current opacities are insufficient to model it.

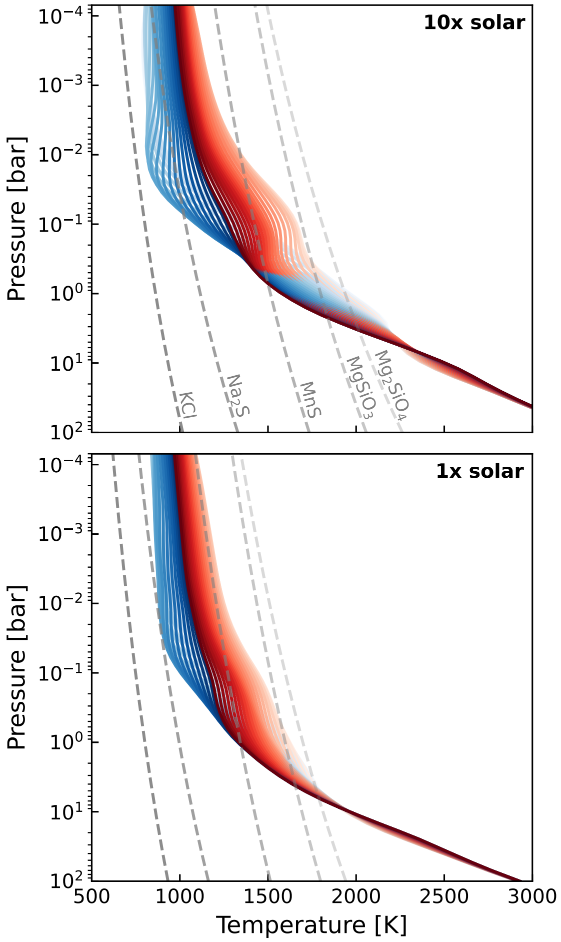

Figure 7. PT profiles derived from cloud-free UM GCM simulations of WASP-96 b at solar (bottom) and 10× solar (top) metallicity, which bracket our derived atmosphere composition. Blue and red profiles represent the morning and evening hemispheres, respectively. Levels of fading denote latitude, with the boldest colors being polar latitudes. Condensation curves for prominent condensate species (labeled) are shown with gray dashed lines.

Alternatively, the slope in our data could be attributed to the effects of stellar contamination via the transit light source effect (TLSE; B. V. Rackham et al. 2018, 2019). We explore this possibility with `Aurora`, this time adding a stellar contamination parameterization (following, e.g., M. Fournier-Tondreau et al. 2024) to the baseline model. In this case, we find that a star with ∼5% spot coverage (at $T_{\text{spot}} \approx 3900$ K) can provide a slope across the VLT and JWST bandpass that can mimic the scattering effects of an aerosol layer. In this case, the effects of the aerosol layer are significantly weaker and consistent with Rayleigh-like scattering in the atmosphere of WASP-96 b. Additionally, the inferred stellar parameters are consistent with expectations for a late G-type star like WASP-96 (B. V. Rackham et al. 2019), making this another plausible explanation for the transmission spectrum slope.

On the other hand, when L.-C. Wang et al. (2026) jointly analyzed a re-reduction of the NIRISS/SOSS observations with the VLT transit data, they found a NIRISS spectrum significantly flatter than those produced in this work (or used in M. Radica et al. 2023 and J. Taylor et al. 2023). They interpreted the data to show evidence for aerosols, but in the form of gray cloud opacity rather than a scattering slope, since their spectrum did not display an optical slope. They note that this difference may be due to the use of newer calibration reference files than were available to earlier studies. However, here we have also made use of the most up-to-date calibration files available from the CRDS, and so this is unlikely to be the true driver of the differences between the two spectra. We note, however, that although L.-C. Wang et al. (2026) carry out a group-level $1/f$ correction in their reanalysis, they do not do a group-level background subtraction, which, as shown by M. Radica et al. (2023), can cause substantial wavelength-dependent biases. Determining whether that is the ultimate cause of the differences between our analysis and theirs is beyond the scope of this work.

5. Exploration of Morning–Evening Limb Asymmetry

WASP-96 b should be a strong candidate for observable morning–evening limb asymmetry (D. Samra et al. 2023; M. M. Murphy et al. 2024a; M. Zamyatina et al. 2024). M. Zamyatina et al. (2024), in particular, explored the observability of limb asymmetry on WASP-96 b using the Met Office's `Unified Model` (UM) GCM, finding the potential for up to 500 ppm differences between the morning and evening limbs, depending on the assumed metallicity and whether or not the planet's atmosphere is in chemical equilibrium.

From Figure 3, the morning and evening spectra show hints of asymmetry. Though very low S/N, the morning spectrum appears flatter across the full wave band explored, whereas the evening spectrum shows suggestions of features, particularly around 1.4 and 4.5 μm where H_2O and CO_2 absorb. We also show the T_0 spectrum in the bottom panel of Figure 3, derived from spectroscopic fits to the transit light curves assuming a uniform planet (i.e., a `batman` model) and allowing the midtransit time to vary. We see evidence for the same midtransit time offset in the Na feature as L.-C. Wang et al. (2026); though, this is the lowest-S/N part of the data and thus potentially the least reliable region to constrain limb asymmetry.

Inspired by recent studies finding evidence for clear evening and cloudy morning limbs on giant exoplanets (e.g., S. Mukherjee et al. 2025b; M. M. Murphy et al. 2025; G. Fu et al. 2025) we explore the possibility for WASP-96 b to have asymmetric cloud coverage on its limbs using the UM GCM. Specific details of the GCM setup can be found in Appendix C, and we show generated PT profiles in Figure 7 at two representative metallicities. We also overplot condensation curves from C. V. Morley et al. (2012) and C. Visscher et al. (2010) for some prominent condensate species. The UM PT profiles support the condensation of species like Na_2S at ∼mbar levels on the cooler morning terminator, whereas the comparatively warmer evening terminator would remain relatively cloud free. This is in rough agreement with the findings of D. Samra et al. (2023) who concluded that mild asymmetry is possible in WASP-96 b's atmosphere for a variety of condensate compositions. We also overplot morning and evening limb-averaged spectra from the aerosol-free 10× solar UM GCM run in purple in Figure 3. The model provides an excellent match to the evening spectrum, but overpredicts feature sizes in the morning.

5.1. Toward a More Robust Quantification of Transit Limb Asymmetry

The above discussion is only circumstantial evidence for limb asymmetry in WASP-96 b. The question arises of how to robustly quantify the presence of limb asymmetry, particularly in low-S/N cases like the present one. The T_0 spectrum is an excellent tracer of limb asymmetry as variation in the midtransit time can only be caused by changes in shape of the planet when all else is held fixed (S. Seager & G. Mallen-Ornelas 2003; N. Espinoza & K. Jones 2021; M. M. Murphy et al. 2024a). But these spectra can also be low S/N (as in the present case), and only really yield “by-eye” evidence. On the opposite end of the spectrum, Bayesian model comparison tests have been performed on light curves in order to determine whether there is sufficient evidence for an asymmetric `catwoman` model over a symmetric `batman` one (e.g., E.-M. Ahrer et al. 2025b). As in E.-M. Ahrer et al. (2025b), we find that the symmetric model is strongly favored ($\ln B \gtrsim 5$) for WASP-96 b at all wavelengths. However, this test is not ideal as it does not take into account wavelength-dependent information (i.e., the presence and lack of spectral features).

Here, we suggest some tests to quantify the degree to which morning and evening spectra show feature differences. We first perform a Gaussian feature test (e.g., E. M. May et al. 2023; S. E. Moran et al. 2023; J. Taylor et al. 2025) on the morning and evening spectra. Following the methods of J. Taylor et al. (2025), we compare two models: a flat line (one free parameter; an offset) and a model with a single Gaussian feature (four free parameters; an offset, Gaussian feature position, amplitude, and width). We treat the NIRISS and NIRSpec separately on account of the potential for an offset between them. Using `dynesty` (J. S. Speagle 2020), we fit each model to the morning and evening spectra from each instrument and calculate the associated Bayesian evidence values.

For the morning spectra, the flat line model is strongly preferred ($\ln B > 3.5$) for both instruments over the presence of a Gaussian feature, supporting the claim that both are featureless. On the other hand, the test finds weak-to-moderate evidence ($\ln B = 1.36$) for a Gaussian bump at 4.5 μm in the NIRSpec evening spectrum compared to a flat line. The NIRISS evening spectrum shows marginal evidence for a Gaussian feature at ~1.4 μm ($\ln B = 0.76$) over a flat line; though, this increases to $\ln B = 1.21$ if we force the feature to be at 1.4 μm instead of allowing the prior to span the whole SOSS wave band. This test is also not entirely foolproof. It works if one limb is entirely featureless whereas the other shows features. However, it would not be informative when features are present in both limbs.

Next, we try another test to address these shortcomings that builds off of the work of G. Fu et al. (2025). We define a spectral amplitude index, A_H, which quantifies the difference in transit depth inside and outside of a spectral feature:

$$A_H = (\text{in} - \text{band} - \text{out} - \text{of} - \text{band})/\text{error}. \tag{1}$$

We focus on the NIRISS 1.4 μm H_2O band (in-band: 1.35–1.5 μm, out-of-band: 0.9–1.3 μm, shaded blue and gray, respectively, in Figure 3) the same as in G. Fu et al. (2025). The in- and out-of-band values are band averages in atmosphere scale heights, and the errors are propagated from the individual transit depths and added in quadrature (G. Fu et al. 2025). We calculate A_H separately for the morning and evening limbs and then subtract them to quantify the difference in the H_2O-band amplitude,

$$\delta A_H = A_{H,\text{evening}} - A_{H,\text{morning}}. \tag{2}$$

The value for WASP-96 b is δA_H=2.13±0.31.

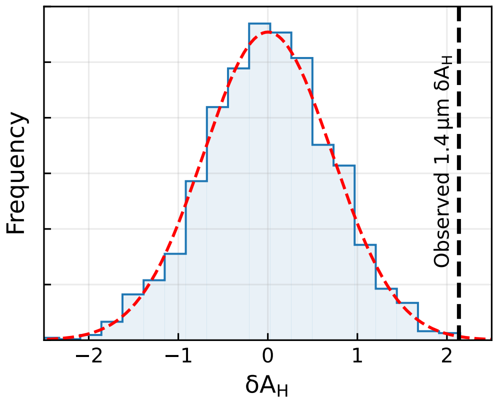

Figure 8. Distribution of δA_H values from 10,000 injection-recovery tests with no underlying limb asymmetry. The red dashed curve shows the best-fitting Gaussian distribution ($\mu = -0.012$, $\sigma = 0.717$). The observed δA_H (black dashed line) for the 1.4 μm H_2O band of 2.13 is in the 99.72th percentile of the distribution, making it a ~2.6σ outlier. Read another way, potential morning–evening asymmetry around 1.4 μm is ~2.6σ significant based on this test.

Next, we compare to the distribution of δA_H values in the absence of any underlying asymmetry. To this end, we simulate 10,000 sets of light curves with the same noise and transit properties as WASP-96 b, except that the planet is uniform (i.e., no limb asymmetry). We then fit these light curves with `catwoman` to obtain limb spectra and calculate δA_H for each case as was done above. The calculated distribution of δA_H values is shown in Figure 8 and is well described by a Gaussian centered on zero, with a width of 0.72. This analysis suggests that differences of this size can arise stochastically at low S/N. However, asymmetry in the 1.4 μm band at the level we see is a 2.6σ outlier in the derived distribution. Read another way, the potential 1.4 μm feature asymmetry is 2.6σ significant via this test. We also explore using the 4.5 μm CO_2 feature for this test and find similar but weaker results, primarily due to the lower overall S/N in this region.

Again, this test is not entirely foolproof. For example, it would be inappropriate in cases where limb differences are solely due to temperature or where suitable out-of-band wavelengths cannot be identified. We suggest that the development of a robust and widely applicable quantification scheme for limb asymmetry should be a community priority. For example, “leave-one-out” cross-validation techniques (e.g., R. Cloutier et al. 2019; M. Radica et al. 2022b) recently adapted for the interpretation of atmospheric models and inferences (L. Welbanks et al. 2023; M. C. Nixon et al. 2024) could potentially be applied to the interpretation of limb asymmetries, building on the work of R. C. Challener et al. (2023) for eclipse mapping.

6. Conclusions

In this work we conducted an in-depth characterization of the atmosphere of WASP-96 b, building off of the work by M. Radica et al. (2023) and J. Taylor et al. (2023). We combined archival VLT/FORS2 and JWST NIRISS/SOSS with new NIRSpec/G395H transit observations to create a high precision 0.35–5 μm atmosphere spectrum, and we summarize the major findings of our analysis below.

1. We obtain strong detections of H_2O, CO_2, and Na in free retrievals; however, CO remains unconstrained. Free retrievals thus indicate a broadly superstellar metallicity (lower limits of 2–8× solar or 1–4× stellar depending on the particular retrieval code). With CO included self-consistently, the `ScCHIMERA` grid yields a metallicity of 4–12× solar (2–6× stellar).
2. We find a moderate ($\ln B$=2.69) preference in free retrievals for models with SO_2 versus those without. The retrieved abundance agrees with photochemical predictions, and WASP-96 b falls right on the SO_2 shoreline proposed by I. J. M. Crossfield et al. (2025).
3. Our chemical equilibrium retrievals and self-consistent grids yield a substellar-to-stellar C/O ratio. When combined with our metallicity constraints, this potentially indicates formation beyond the H_2O snowline and the accretion of volatile-rich material.
4. Our atmosphere spectrum displays a strong slope bluewards of ∼1.5 μm, which our models explain via aerosol scattering opacity. Small-particle condensate clouds or photochemically produced hazes can potentially cause this slope; though, we also cannot entirely rule out the broad wings of the Na feature or stellar contamination. Further observations should be conducted to disentangle/uniquely identify these factors.
5. We explore the possibility for limb asymmetry in the atmosphere of WASP-96 b, but do not find conclusive evidence one way or the other. We encourage the community to prioritize the development of a metric to quantify the presence of limb asymmetry, and we present some suggestions in this direction.
6. Finally, we demonstrate that removing $1/f$ noise in JWST NIRISS/SOSS observations after ramp fitting (i.e., at the integration level) can inject an optical-to-NIR slope and excess covariance into transmission spectra compared to a group-level correction.

Our identification of SO_2 is not definitive and should be followed up with JWST MIRI/LRS observations, which are incredibly sensitive to SO_2 (e.g., A. Dyrek et al. 2024; D. Powell et al. 2024) as well as cloud-induced limb asymmetry (e.g., M. M. Murphy et al. 2025). Moreover, MIRI observations would provide definitive evidence for aerosols via the identification of specific absorption features (H. R. Wakeford & D. K. Sing 2015; D. Grant et al. 2023). Finally, we reiterate our encouragement that the community be thoughtful and thorough when reporting limb asymmetry detections or lack thereof—particularly in low-S/N regimes.

Acknowledgments

M.R. would like to acknowledge funding from the Natural Sciences and Engineering Research Council of Canada (NSERC), as well as the Canadian Space Agency (CSA). J. T. was supported by the Glasstone Benefaction, University of Oxford (Violette and Samuel Glasstone Research Fellowships in Science 2024). D.C. receives funding from the Max Planck Society. N.J.M. and M.Z. acknowledge support from a UKRI Future Leaders Fellowship [grant MR/T040866/1], a Science and Technology Facilities Funding Council Nucleus Award [grant ST/T000082/1], and the Leverhulme Trust through a research project grant [RPG-2020-82]. J.B. acknowledges the support received in part from the NYUAD IT High Performance Computing resources, services, and staff expertise. This work is based on observations made with the NASA/ESA/CSA JWST. The data were obtained from the Mikulski Archive for Space Telescopes at the Space Telescope Science Institute, which is operated by the Association of Universities for Research in Astronomy, Inc., under NASA contract NAS 5-03127 for JWST. The specific observations analyzed can be accessed via DOI: 10.17909/g5qz-cv38. This research has made use of the NASA Exoplanet Archive (J. L. Christiansen et al. 2025), which is operated by the California Institute of Technology, under contract with the National Aeronautics and Space Administration under the Exoplanet Exploration Program.

Facilities: JWST (NIRISS), JWST (NIRSpec).

Software: `astropy` (Astropy Collaboration et al. 2013, 2018), `batman` (L. Kreidberg 2015), `catwoman` (K. Jones & N. Espinoza 2020; N. Espinoza & K. Jones 2021), `dynesty` (J. S. Speagle 2020), `emcee` (D. Foreman-Mackey et al. 2013), `ipython` (F. Pérez & B. E. Granger 2007), `jwst` (H. Bushouse et al. 2023), `matplotlib` (J. D. Hunter 2007), `numpy` (C. R. Harris et al. 2020), `pymultinest` (J. Buchner 2016), `scipy` (P. Virtanen et al. 2020).

Appendix A
Additional Data Reductions

A.1. NIRISS/SOSS: `NAMELESS`

We perform an independent reduction of the NIRISS/SOSS TSO using the `NAMELESS` pipeline (L.-P. Coulombe et al. 2023, 2025), following closely the methodology applied in L.-P. Coulombe et al. (2025). We start from the raw uncalibrated data and proceed through the Stage 1 and 2 steps of the `jwst` pipeline, up to flat-field correction. We then flag bad/hot pixels by isolating pixels with large 2D second derivatives and correct for them via 2D cubic interpolation. We correct for the nonuniform background by scaling independently the two portions of the STScI model background separated by the sharp jump in flux, and subtract it from all integrations (O. Lim et al. 2023). Remaining cosmic rays are corrected for by computing the running median of all individual pixels and bringing all counts $>4\sigma$ to the median value. The $1/f$ noise is computed and subtracted by scaling each column of each trace independently and determining the $1/f$ within the trace via χ^2 minimization, following the same method outlined in L.-P. Coulombe et al. (2025). Finally, we extract the stellar spectra using a fixed box width of 36 pixels.

We proceeded to fit the spectrophotometric light curves using `exoUPRF` (M. Radica 2024b; E.-M. Ahrer et al. 2025a; M. Radica et al. 2025b) and following the same procedure as for the `exoTEDRF` spectrum (see Section 2.4), thereby ensuring that any differences in the transmission spectra were due to choices made during the reduction process and not introduced as part of the light curve fitting.

A.2. NIRSpec/G395H: `Eureka!`

For a second independent reduction of our data we used the `Eureka!` pipeline (T. Bell et al. 2022), closely following the procedures used in other NIRSpec/G395H reductions of hot

Jupiters (e.g., E.-M. Ahrer et al. 2025b; J. Kirk et al. 2025). For the first step, we used the uncalibrated fits files and followed the default steps of the `jwst` pipeline (H. Bushouse et al. 2023) for Stages 1 and 2, with the exception of using a 10σ threshold for the `jump_rejection_threshold`, using a scaling factor for the superbias to calibrate it, and subtracting a column-by-column weighted average at the group-level (masking the trace). After ramp fitting, we ran Stage 3, which extracts the time-series spectra. We used a 5σ threshold for spatial outlier rejection and a double-iterative 5σ threshold along the time axis. We corrected for the curvature of the spectral trace and used pixels >8 pixels from the central trace pixels for a column-by-column weighted average background subtraction. To extract the final 1D spectra we used optimal extraction (K. Horne 1986) with an aperture half width of four pixels.

We used the same wavelength bins at $R=100$ and $R=300$ as the `exoTEDRF` reduction to produce the spectroscopic light curves of the transit of WASP-96 b. Using `Eureka!`'s Stage 4 we masked outliers in the binned light curves using a $>5\sigma$ threshold, a 20 pixel rolling median and five iterations. The extracted light curves are then fitted within Stage 5 using a `batman` transit model (L. Kreidberg 2015) and a linear in time. We use the four-parameter limb-darkening law and fix the parameters $u1$, $u2$, $u3$, $u4$ to the generated values using `ExoTiC-LD` (D. Grant & H. R. Wakeford 2024) following the parameters for WASP-96 ($T_{\rm eff}=5500$ K, $\rm M/H=0.14$, $\log g=4.42$; C. Hellier et al. 2014) and the `stagger` grid (Z. Magic et al. 2015). We fix the system parameters to the best-fit parameters from the joint fit; see Table 1. Therefore our spectroscopic light curve fits consisted of four free parameters: the transit depth, two parameters for the linear and a free parameter for error inflation. We use the MCMC python package `emcee` (D. Foreman-Mackey et al. 2013) for our light curve fits. The `Eureka!` transmission spectrum at $R=300$ is compared to the `exoTEDRF` one in Figure 2.

Appendix B
On the Correction of 1/f Noise for NIRISS/SOSS

As shown in Figure 2, there are significant differences between the `exoTEDRF` and `NAMELESS` NIRISS/SOSS spectra redwards of $\sim$1.7 μm, despite the excellent agreement at bluer wavelengths. Such differences have also been observed in other studies of giant planets (e.g., M. Radica et al. 2023; M. Fournier-Tondreau et al. 2024), but not in multiple studies of smaller planets (e.g., O. Lim et al. 2023; M. Radica et al. 2025b; B. Benneke et al. 2024) and/or brighter stars (e.g., M. Radica et al. 2024; E.-M. Ahrer et al. 2025a). We could not trace this deviation back to differences in light curve fitting, which led to a reassessment of the choices made in the data reduction itself.

One major difference between the standard `exoTEDRF` and `NAMELESS` workflows is the correction of $1/f$ noise at the group- versus the integration level (that is, before or after ramp fitting). We thus perform an experiment where we redo the `exoTEDRF` data reduction, but skip the group-level $1/f$ correction and instead perform the same step after ramp fitting, analogous to how it is carried out with `NAMELESS`. As shown in Figure 9 this new `exoTEDRF` spectrum is in much better agreement with `NAMELESS` and qualitatively reproduces the deviations seen with the nominal `exoTEDRF` spectrum.

Though the proximate cause seems to be the order in which one performs the $1/f$ correction and ramp fitting, at this time the ultimate cause of these deviations is still unclear. The fact that they only appear (or potentially just appear more clearly) in datasets with deep transits, which target dimmer stars, and are largest where the instrument throughput is smallest suggest some type of diluting effect. However, despite extensive testing, we have not been able to confirm this hypothesis nor identify its root cause.

In Figure 10 we show covariance matrices for the nominal `exoTEDRF` spectrum, as well as the `NAMELESS` spectrum and the reprocessed `exoTEDRF` with integration-level $1/f$ correction. The off-diagonal structures first noted by M. Holmberg & N. Madhusudhan (2023) are present in the latter two, but disappear when performing the $1/f$ correction at the group level. These off-diagonal covariances are introduced by the $1/f$ correction, which in the three examples shown here (as well as M. Holmberg & N. Madhusudhan 2023) subtracts a single $1/f$ value from each detector column, thereby introducing correlations between wavelengths in the first and second diffraction orders that share a given column. However, when $1/f$ noise is subtracted at the group level, the ramp fitting erases much of these correlations yielding an almost purely diagonal, and thus ideal, covariance.

Although we do not necessarily know the ground truth for any exoplanet transit spectrum, and it is impossible to simulate noise sources or systematics that are not well understood, we nevertheless concur with A. L. Carter et al. (2025) and argue that the group-level $1/f$ correction is the most proper method—and is indeed how this noise source is treated for JWST's other science instruments (e.g., L. Alderson et al. 2023; Z. Rustamkulov et al. 2023). First, $1/f$ noise is one of the last to be imparted on the data as it is injected during readout and thus should be one of the first to be removed during the data reduction. The group-level $1/f$ correction leads to lower light curve scatter and smaller final error bars (e.g., M. Radica et al. 2023), and finally, leaves negligible off-diagonal covariance in the data—metrics that have been widely employed throughout the history of the field to determine the "optimal" data treatment.

Appendix C
Details of the UM GCM Simulations

To provide an additional point of comparison for our observations, we simulate the atmosphere of WASP-96 b using the Met Office's UM GCM, which has modeled hot Jupiters and Saturns previously and been specifically used to model the atmosphere of WASP-96 b in J. Taylor et al. (2023) and M. Zamyatina et al. (2024). The UM solves the full, deep-atmosphere Euler equations (see N. Wood et al. 2014 and N. J. Mayne et al. 2014 for a discussion of implementation) with multiband radiative transfer handled using the `socrates` radiative transfer code (J. M. Edwards & A. Slingo 1996). The atmosphere is assumed to have 1× or 10× solar metallicity and with the chemical abundances initially set to be in thermochemical equilibrium. The evolution of the abundances are followed using the UM's chemical kinetics solver using the O. Venot et al. (2019) C/N/O/H network, allowing for the possibility that the chemical abundances diverge from equilibrium. A subset of these chemical species contributes opacity to the gas: H_2O, CO,

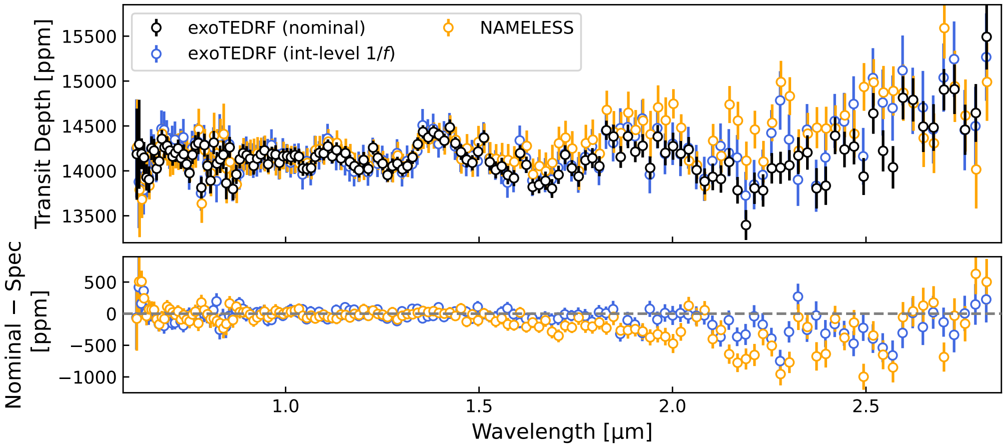

Figure 9. The differences between the `exoTEDRF` and `NAMELESS` NIRISS/SOSS spectra redwards of ∼1.75 μm can be attributed to the $1/f$ noise correction being performed at the integration vs. the group level (i.e., after vs. before ramp fitting). An alternate `exoTEDRF` reduction skipping the group level $1/f$ correction and implementing the same step at the integration level reproduces qualitatively the differences with the nominal spectrum seen with `NAMELESS`.

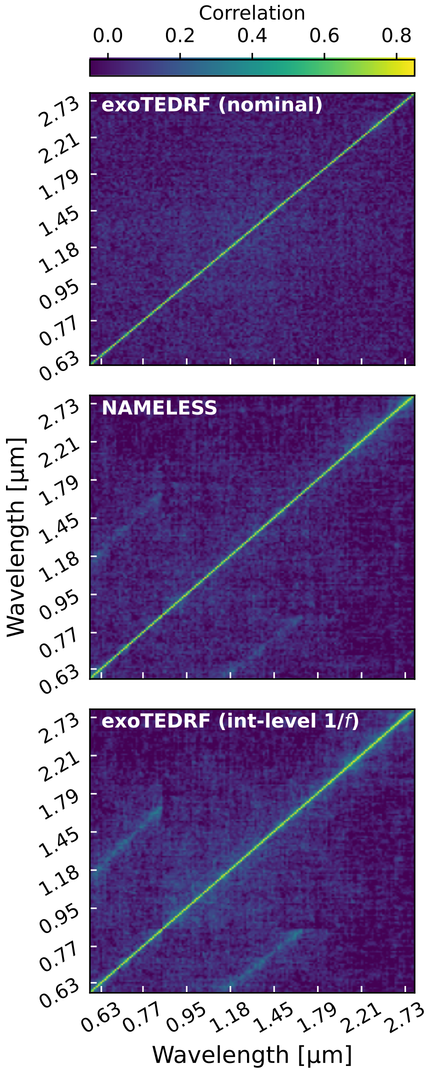

Figure 10. Covariance matrices extracted from the NIRISS/SOSS light curve fit residuals for the nominal `exoTEDRF` reduction (top), the `NAMELESS` reduction (middle), and the alternate `exoTEDRF` reduction performing an integration-level $1/f$ noise correction (bottom). Significant residual covariance between wavelengths that share a detector column are present when performing the $1/f$ noise correction at the integration level, but not for the group-level correction.

Table 3
GCM Parameters

	Value
Grid and Domain	
Longitude Cells	144
Latitude Cells	90
Vertical Layers	86
Domain Height	1.01×10^7 m
Domain Inner Radius	7.86×10^7 m
Hydrodynamic Time Step	30 s
Radiative Transfer	
Wavelength Bins	32
Wavelength Minimum	0.2 μm
Wavelength Maximum	322 μm
Radiative Time step	150 s
Damping and Diffusion	
Damping Profile	Horizontally Uniform
Damping Coefficient	0.15
Damping Depth (η_s)	0.8
Planet	
Intrinsic Temperature	100 K
Initial Inner Boundary Pressure	200 bar
Semimajor axis a	4.53×10^{-2}au
Stellar Constant at 1 au	1272 W m^{-2}
Specific Gas Constant R	3164.7 J kg^{-1}K^{-1}
Specific Heat Capacity $c_{\rm P}$	11476.7 J kg^{-1}K^{-1}
g at Inner Boundary	10.04 m s^{-2}

CO$_2$, CH$_4$, NH$_3$, HCN, Li, Na, K, Rb, and Cs as well as CIA by H$_2$-H$_2$ and H$_2$-He and Rayleigh scattering by H$_2$ and He.

The simulation was run for 1000 Earth days, and the final output is used for the analyses here. Extended details of the GCM setup are presented in Table 3.

Appendix D
Retrieval Summaries and Example Corner Plots

Table 4 has citations for all opacity sources used in our atmosphere models. Figure 11 shows the corner plot from the `POSEIDON` retrieval on the combined $R = 300$ `exoTEDRF` JWST + VLT spectrum. Corner plots from all other retrievals are available on Zenodo.

Table 4

Opacity Sources and References

Parameter	`POSEIDON`	`NemesisPy`	`Pyrat Bay`	`Aurora`	`ScCHIMERA`
H_2O	O. L. Polyansky et al. (2018)	“ ”	L. S. Rothman et al. (2010)	O. L. Polyansky et al. (2018)	“ ”
CO_2	S. N. Yurchenko et al. (2020)	“ ”	L. S. Rothman et al. (2010)	“ ”	R. S. Freedman et al. (2014)
CO	G. Li et al. (2015)	“ ”	“ ”	L. S. Rothman et al. (2010)	“ ”
CH_4	S. N. Yurchenko et al. (2024)	“ ”	R. J. Hargreaves et al. (2020)	S. N. Yurchenko et al. (2024)	L. S. Rothman et al. (2010)
SO_2	D. S. Underwood et al. (2016)	“ ”	“ ”	“ ”	“ ”
H_2S	A. A. A. Azzam et al. (2016)	“ ”	—	—	“ ”
HCN	R. J. Barber et al. (2014)	“ ”	G. J. Harris et al. (2006)	R. J. Barber et al. (2014)	“ ”
NH_3	P. A. Coles et al. (2019)	“ ”	S. N. Yurchenko et al. (2011)	“ ”	P. A. Coles et al. (2019)
Na	T. Ryabchikova et al. (2015)	N. F. Allard et al. (2019)	“ ”	“ ”	“ ”
K	T. Ryabchikova et al. (2015)	N. F. Allard et al. (2016)	“ ”	“ ”	“ ”
C_2H_2	—	—	—	—	K. L. Chubb et al. (2020)
H_2-H_2	K. L. Chubb et al. (2021)	A. Borysow et al. (2001), A. Borysow (2002)	“ ”	C. Richard et al. (2012)	R. S. Freedman et al. (2008)
H_2-He	K. L. Chubb et al. (2021)	A. Borysow & L. Frommhold (1989), A. Borysow et al. (1989)	“ ”	C. Richard et al. (2012)	R. S. Freedman et al. (2008)

Note. “—” indicates that a parameter was not included in a retrieval. “ ” denotes a repeat of the previous column.

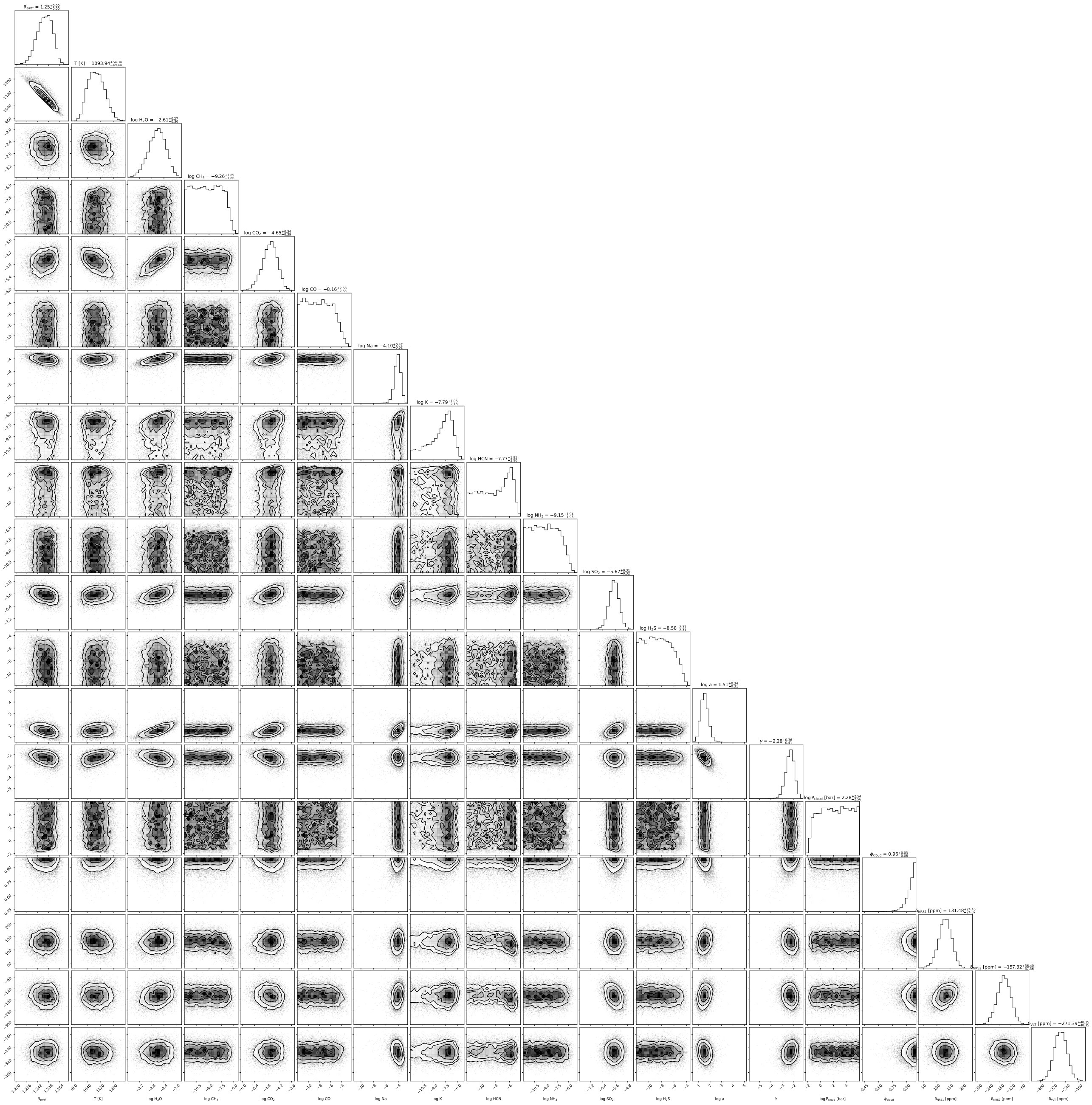

Figure 11. Corner plot from the `POSEIDON` retrieval on the combined VLT + `exoTEDRF`$R = 300$ JWST spectrum.

ORCID iDs

Michael Radica https://orcid.org/0000-0002-3328-1203
Jake Taylor https://orcid.org/0000-0003-4844-9838
Yoav Rotman https://orcid.org/0000-0003-4459-9054
Jasmina Blecic https://orcid.org/0000-0002-0769-9614
Luis Welbanks https://orcid.org/0000-0003-0156-4564
Eva-Maria Ahrer https://orcid.org/0000-0003-0973-8426
Duncan Christie https://orcid.org/0000-0002-4997-0847
Louis-Philippe Coulombe https://orcid.org/0000-0002-2195-735X
Gillis Lowry https://orcid.org/0009-0007-1562-2944
Matthew M. Murphy https://orcid.org/0000-0002-8517-8857
Adina D. Feinstein https://orcid.org/0000-0002-9464-8101
David Lafrenière https://orcid.org/0000-0002-6780-4252
Ryan J. MacDonald https://orcid.org/0000-0003-4816-3469
Nathan J. Mayne https://orcid.org/0000-0001-6707-4563
Shang-Min Tsai https://orcid.org/0000-0002-8163-4608
Maria Zamyatina https://orcid.org/0000-0002-9705-0535

References

Ahrer, E.-M., Gandhi, S., Alderson, L., et al. 2025b, MNRAS, 540, 2535
Ahrer, E.-M., Radica, M., Piaulet-Ghorayeb, C., et al. 2025a, ApJL, 985, L10
Ahrer, E.-M., Stevenson, K. B., Mansfield, M., et al. 2023, Natur, 614, 653
Albert, L., Lafrenière, D., René, D., et al. 2023, PASP, 135, 075001
Alderson, L., Wakeford, H. R., Alam, M. K., et al. 2023, Natur, 614, 664
Ali-Dib, M. 2017, MNRAS, 467, 2845
Allard, N. F., Spiegelman, F., & Kielkopf, J. F. 2016, A&A, 589, A21
Allard, N. F., Spiegelman, F., Leininger, T., & Molliere, P. 2019, A&A, 628, A120
Allart, R., Coulombe, L.-P., Carteret, Y., et al. 2025, NatCo, 16, 10822

Asplund, M., Grevesse, N., Sauval, A. J., & Scott, P. 2009, ARA&A, 47, 481

Astropy Collaboration, Price-Whelan, A. M., Sipőcz, B. M., et al. 2018, AJ, 156, 123

Astropy Collaboration, Robitaille, T. P., Tollerud, E. J., et al. 2013, A&A, 558, A33

Atreya, S. K., Crida, A., Guillot, T., et al. 2022, arXiv:2205.06914

Azzam, A. A. A., Tennyson, J., Yurchenko, S. N., & Naumenko, O. V. 2016, MNRAS, 460, 4063

Barber, R. J., Strange, J. K., Hill, C., et al. 2014, MNRAS, 437, 1828

Barstow, J. K., Aigrain, S., Irwin, P. G. J., & Sing, D. K. 2017, ApJ, 834, 50

Bell, T., Ahrer, E.-M., Brande, J., et al. 2022, JOSS, 7, 4503

Bell, T. J., Welbanks, L., Schlawin, E., et al. 2023, Natur, 623, 709

Benneke, B., Roy, P.-A., Coulombe, L.-P., et al. 2024, arXiv:2403.03325

Birkmann, S. M., Ferruit, P., Giardino, G., et al. 2022, A&A, 661, A83

Borysow, A. 2002, A&A, 390, 779

Borysow, A., & Frommhold, L. 1989, ApJ, 341, 549

Borysow, A., Frommhold, L., & Moraldi, M. 1989, ApJ, 336, 495

Borysow, A., Jorgensen, U. G., & Fu, Y. 2001, JQRST, 68, 235

Buchner, J. 2016, S&C, 26, 383

Buchner, J., Georgakakis, A., Nandra, K., et al. 2014, A&A, 564, A125

Bushouse, H., Eisenhamer, J., Dencheva, N., et al. 2023, JWST Calibration Pipeline, v1.12.3, Zenodo, doi:10.5281/zenodo.8404029

Carter, A. L., Espinoza, N., Albert, L., et al. 2025, Effects of Jump Detection and Ramp Fitting Algorithms on NIRISS/SOSS Exoplanet Time-Series Observations JWST-STSSTScIcI-008975, STScI

Carter, A. L., May, E. M., Espinoza, N., et al. 2024, NatAs, 8, 1008

Chachan, Y., Knutson, H. A., Lothringer, J., & Blake, G. A. 2023, ApJ, 943, 112

Challener, R. C., Welbanks, L., & McGill, P. 2023, AJ, 166, 251

Christiansen, J. L., McElroy, D. L., Harbut, M., et al. 2025, PSJ, 6, 186

Chubb, K. L., Rocchetto, M., Yurchenko, S. N., et al. 2021, A&A, 646, A21

Chubb, K. L., Tennyson, J., & Yurchenko, S. N. 2020, MNRAS, 493, 1531

Cloutier, R., Astudillo-Defru, N., Doyon, R., et al. 2019, A&A, 621, A49

Coles, P. A., Yurchenko, S. N., & Tennyson, J. 2019, MNRAS, 490, 4638

Connors, N. J., Monaghan, C., Benneke, B., & Dang, L. 2025, ApJL, 989, L11

Coulombe, L.-P., Benneke, B., Challener, R., et al. 2023, Natur, 620, 292

Coulombe, L.-P., Radica, M., Benneke, B., et al. 2025, NatAs, 9, 512

Cridland, A. J., van Dishoeck, E. F., Alessi, M., & Pudritz, R. E. 2019, A&A, 632, A63

Crossfield, I. J. M. 2023, ApJL, 952, L18

Crossfield, I. J. M., Ahrer, E.-M., Brande, J., et al. 2025, ApJ, 994, 184

Cubillos, P. E., & Blecic, J. 2021, MNRAS, 505, 2675

Darveau-Bernier, A., Albert, L., Talens, G. J., et al. 2022, PASP, 134, 094502

Davenport, B., Kempton, E. M.-R., Nixon, M. C., et al. 2025, ApJL, 984, L44

Doyon, R., Willott, C. J., Hutchings, J. B., et al. 2023, PASP, 135, 098001

Dyrek, A., Min, M., Decin, L., et al. 2024, Natur, 625, 51

Edwards, J. M., & Slingo, A. 1996, QJRMS, 122, 689

Ehrenreich, D., Lovis, C., Allart, R., et al. 2020, Natur, 580, 597

Espinoza, N., Fortney, J. J., Miguel, Y., Thorngren, D., & Murray-Clay, R. 2017, ApJL, 838, L9

Espinoza, N., & Jones, K. 2021, AJ, 162, 165

Espinoza, N., Kossakowski, D., & Brahm, R. 2019, MNRAS, 490, 2262

Espinoza, N., Steinrueck, M. E., Kirk, J., et al. 2024, Natur, 632, 1017

Feinstein, A. D., Radica, M., Welbanks, L., et al. 2023, Natur, 614, 670

Feroz, F., Hobson, M. P., & Bridges, M. 2009, MNRAS, 398, 1601

Fleury, B., Benilan, Y., Venot, O., et al. 2023, ApJ, 956, 134

Foreman-Mackey, D., Hogg, D. W., Lang, D., & Goodman, J. 2013, PASP, 125, 306

Fournier-Tondreau, M., MacDonald, R. J., Radica, M., et al. 2024, MNRAS, 528, 3354

Freedman, R. S., Lustig-Yaeger, J., Fortney, J. J., et al. 2014, ApJS, 214, 25

Freedman, R. S., Marley, M. S., & Lodders, K. 2008, ApJS, 174, 504

Fu, G., Mukherjee, S., Stevenson, K. B., et al. 2025, ApJL, 989, L17

Fu, G., Welbanks, L., Deming, D., et al. 2024, Natur, 632, 752

Fulton, B. J., Petigura, E. A., Blunt, S., & Sinukoff, E. 2018, PASP, 130, 044504

Gandhi, S., Kesseli, A., Snellen, I., et al. 2022, MNRAS, 515, 749

Gordon, S., & Mcbride, B. J. 1994, Computer program for calculation of complex chemical equilibrium compositions and applications. Part 1: Analysis 19950013764, NASA Lewis Research Center

Grant, D., Lewis, N. K., Wakeford, H. R., et al. 2023, ApJL, 956, L29

Grant, D., & Wakeford, H. R. 2024, JOSS, 9, 6816

Greene, T. P., Bell, T. J., Ducrot, E., et al. 2023, Natur, 618, 39

Hargreaves, R. J., Gordon, I. E., Rey, M., et al. 2020, ApJS, 247, 55

Harris, C. R., Millman, K. J., van der Walt, S. J., et al. 2020, Natur, 585, 357

Harris, G. J., Tennyson, J., Kaminsky, B. M., Pavlenko, Y. V., & Jones, H. R. A. 2006, MNRAS, 367, 400

Hellier, C., Anderson, D. R., Cameron, A. C., et al. 2014, MNRAS, 440, 1982

Holmberg, M., & Madhusudhan, N. 2023, MNRAS, 524, 377

Horne, K. 1986, PASP, 98, 609

Hunter, J. D. 2007, CSE, 9, 90

Irwin, P. G. J., Teanby, N. A., de Kok, R., et al. 2008, JQRST, 109, 1136

Jeffreys, H. 1935, PCPS, 31, 203

Jenkins, J. M., Twicken, J. D., McCauliff, S., et al. 2016, SPIE, 9913, 99133E

Jones, K., & Espinoza, N. 2020, JOSS, 7, 2382

Kempton, E. M.-R., Bean, J. L., Louie, D. R., et al. 2018, PASP, 130, 114401

Kempton, E. M.-R., Zhang, M., Bean, J. L., et al. 2023, Natur, 620, 67

Kipping, D. M. 2013, MNRAS, 435, 2152

Kirk, J., Ahrer, E.-M., Claringbold, A. B., et al. 2025, MNRAS, 537, 3027

Kokori, A., Tsiaras, A., Edwards, B., et al. 2023, ApJS, 265, 4

Kreidberg, L. 2015, PASP, 127, 1161

Krishnamurthy, V., Carteret, Y., Piaulet-Ghorayeb, C., et al. 2025, NatAs, 10, 258

Lacis, A. A., & Oinas, V. 1991, JGR, 96, 9027

Lecavelier Des Etangs, A., Pont, F., Vidal-Madjar, A., & Sing, D. 2008, A&A, 481, L83

Li, G., Gordon, I. E., Rothman, L. S., et al. 2015, ApJS, 216, 15

Lim, O., Benneke, B., Doyon, R., et al. 2023, ApJL, 955, L22

Line, M. R., & Parmentier, V. 2016, ApJ, 820, 78

Line, M. R., Wolf, A. S., Zhang, X., et al. 2013, ApJ, 775, 137

Lodders, K., Palme, H., & Gail, H.-P. 2009, LanB, 4B, 712

Lothringer, J. D., Rustamkulov, Z., Sing, D. K., et al. 2021, ApJ, 914, 12

Louie, D. R., Mullens, E., Alderson, L., et al. 2025, AJ, 169, 86

Luque, R., Piaulet-Ghorayeb, C., Radica, M., et al. 2025, A&A, 700, A284

MacDonald, R. J. 2023, JOSS, 8, 4873

MacDonald, R. J., & Madhusudhan, N. 2017, MNRAS, 469, 1979

Madhusudhan, N. 2012, ApJ, 758, 36

Madhusudhan, N., Amin, M. A., & Kennedy, G. M. 2014, ApJ, 794, L12

Madhusudhan, N., Sarkar, S., Constantinou, S., et al. 2023, ApJL, 956, L13

Madhusudhan, N., & Seager, S. 2009, ApJ, 707, 24

Magic, Z., Chiavassa, A., Collet, R., & Asplund, M. 2015, A&A, 573, A90

Mansfield, M., Bean, J. L., Oklopčić, A., et al. 2018, ApJ, 868, L34

May, E. M., MacDonald, R. J., Bennett, K. A., et al. 2023, ApJL, 959, L9

Mayne, N. J., Baraffe, I., Acreman, D. M., et al. 2014, A&A, 561, A1

Mcbride, B. J., Gordon, S., & Reno, M. A. 1993, Thermodynamic data for fifty reference elements, https://ntrs.nasa.gov/citations/19930010788

McGruder, C. D., López-Morales, M., Kirk, J., et al. 2022, AJ, 164, 134

McKay, C. P., Pollack, J. B., & Courtin, R. 1989, Icar, 80, 23

Meech, A., Claringbold, A. B., Ahrer, E.-M., et al. 2025, MNRAS, 539, 1381

Moran, S. E., Stevenson, K. B., Sing, D. K., et al. 2023, ApJL, 948, L11

Mordasini, C., van Boekel, R., Mollière, P., Henning, T., & Benneke, B. 2016, ApJ, 832, 41

Morley, C. V., Fortney, J. J., Marley, M. S., et al. 2012, ApJ, 756, 172

Moses, J. I., Visscher, C., Fortney, J. J., et al. 2011, ApJ, 737, 15

Mukherjee, S., Fortney, J. J., Wogan, N. F., Sing, D. K., & Ohno, K. 2025a, ApJ, 985, 209

Mukherjee, S., Sing, D. K., Fu, G., et al. 2025b, arXiv:2505.10910

Murphy, M. M., Beatty, T. G., & Apai, D. 2024a, ApJ, 974, 179

Murphy, M. M., Beatty, T. G., Schlawin, E., et al. 2024b, NatAs, 8, 1562

Murphy, M. M., Beatty, T. G., Schlawin, E., et al. 2025, AJ, 170, 61

Nikolov, N., Sing, D. K., Fortney, J. J., et al. 2018, Natur, 557, 526

Nikolov, N. K., Sing, D. K., Spake, J. J., et al. 2022, MNRAS, 515, 3037

Nixon, M. C., Welbanks, L., McGill, P., & Kempton, E. M.-R. 2024, ApJ, 966, 156

Öberg, K. I., Murray-Clay, R., & Bergin, E. A. 2011, ApJ, 743, L16

Patel, J. A., & Espinoza, N. 2022, AJ, 163, 228

Pelletier, S., Benneke, B., Ali-Dib, M., et al. 2023, Natur, 619, 491

Pelletier, S., Benneke, B., Darveau-Bernier, A., et al. 2021, AJ, 162, 73

Penzlin, A. B. T., Booth, R. A., Kirk, J., et al. 2024, MNRAS, 535, 171

Pérez, F., & Granger, B. E. 2007, CSE, 9, 21

Piaulet-Ghorayeb, C., Benneke, B., Radica, M., et al. 2024, ApJL, 974, L10

Pinhas, A., Rackham, B. V., Madhusudhan, N., & Apai, D. 2018, MNRAS, 480, 5314

Polyansky, O. L., Kyuberis, A. A., Zobov, N. F., et al. 2018, MNRAS, 480, 2597

Powell, D., Feinstein, A. D., Lee, E. K. H., et al. 2024, Natur, 626, 979

Rackham, B. V., Apai, D., & Giampapa, M. S. 2018, ApJ, 853, 122

Rackham, B. V., Apai, D., & Giampapa, M. S. 2019, AJ, 157, 96

Radica, M. 2024a, JOSS, 9, 6898

Radica, M. 2024b, radicamc/exoUPRF: v1.0.1, Zenodo, doi:10.5281/zenodo.12628066

Radica, M., Albert, L., Taylor, J., et al. 2022a, PASP, 134, 104502
Radica, M., Artigau, E., Lafreniére, D., et al. 2022b, MNRAS, 517, 5050
Radica, M., Coulombe, L.-P., Taylor, J., et al. 2024, ApJL, 962, L20
Radica, M., Piaulet-Ghorayeb, C., Taylor, J., et al. 2025b, ApJL, 979, L5
Radica, M., Taylor, J., Wakeford, H. R., et al. 2025a, MNRAS, 538, 1853
Radica, M., Welbanks, L., Espinoza, N., et al. 2023, MNRAS, 524, 835
Richard, C., Gordon, I. E., Rothman, L. S., et al. 2012, JQSRT, 113, 1276
Ricker, G. R., Winn, J. N., Vanderspek, R., et al. 2014, JATIS, 1, 014003
Rothman, L. S., Gordon, I. E., Barber, R. J., et al. 2010, JQSRT, 111, 2139
Rotman, Y., Welbanks, L., Line, M. R., et al. 2025, ApJ, 989, 201
Rustamkulov, Z., Sing, D. K., Mukherjee, S., et al. 2023, Natur, 614, 659
Ryabchikova, T., Piskunov, N., Kurucz, R. L., et al. 2015, PhyS, 90, 054005
Samra, D., Helling, C., Chubb, K. L., et al. 2023, A&A, 669, A142
Seager, S., & Mallen-Ornelas, G. 2003, ApJ, 585, 1038
Seager, S., & Sasselov, D. D. 2000, ApJ, 537, 916
Skilling, J. 2006, BayAn, 1
Spake, J. J., Sing, D. K., Evans, T. M., et al. 2018, Natur, 557, 68
Speagle, J. S. 2020, MNRAS, 493, 3132
Stock, J. W., Kitzmann, D., & Patzer, A. B. C. 2022, MNRAS, 517, 4070
Taylor, J., & Parmentier, V. 2023, MNRAS, 526, 2133
Taylor, J., Radica, M., Chatterjee, R. D., et al. 2025, MNRAS, 540, 3677
Taylor, J., Radica, M., Welbanks, L., et al. 2023, MNRAS, 524, 817
Toon, O. B., McKay, C. P., Ackerman, T. P., & Santhanam, K. 1989, JGR, 94, 16287
Tsai, S.-M., Lee, E. K. H., Powell, D., et al. 2023, Natur, 617, 483
Underwood, D. S., Tennyson, J., Yurchenko, S. N., et al. 2016, MNRAS, 459, 3890
Venot, O., Bounaceur, R., Dobrijevic, M., et al. 2019, A&A, 624, A58
Virtanen, P., Gommers, R., Oliphant, T. E., et al. 2020, NatMe, 17, 261
Visscher, C., Lodders, K., & Fegley, B. 2010, ApJ, 716, 1060
Von Paris, P., Gratier, P., Bordé, P., Leconte, J., & Selsis, F. 2016, A&A, 589, A52
Wakeford, H. R., & Sing, D. K. 2015, A&A, 573, A122
Wakeford, H. R., Visscher, C., Lewis, N. K., et al. 2017, MNRAS, 464, 4247
Wang, L.-C., Rustamkulov, Z., Sing, D. K., et al. 2026, AJ, 171, 147
Welbanks, L., Bell, T. J., Beatty, T. G., et al. 2024, Natur, 630, 836
Welbanks, L., Madhusudhan, N., Allard, N. F., et al. 2019, ApJ, 887, L20
Welbanks, L., & Madhusudhan, N. 2019, AJ, 157, 206
Welbanks, L., & Madhusudhan, N. 2021, ApJ, 913, 114
Welbanks, L., McGill, P., Line, M., & Madhusudhan, N. 2023, AJ, 165, 112
Wiser, L. S., Bell, T. J., Line, M. R., et al. 2025, PNAS, 122, e2416193122
Wogan, N. F., Batalha, N. E., Zahnle, K., et al. 2025, PSJ, 6, 256
Wood, N., Staniforth, A., White, A., et al. 2014, JRMS, 140, 1505
Yang, J., Alday, J., & Irwin, P. 2024, JOSS, 9, 6874
Yip, K. H., Changeat, Q., Edwards, B., et al. 2021, AJ, 161, 4
Yurchenko, S. N., Barber, R. J., & Tennyson, J. 2011, MNRAS, 413, 1828
Yurchenko, S. N., Mellor, T. M., Freedman, R. S., & Tennyson, J. 2020, MNRAS, 496, 5282
Yurchenko, S. N., Owens, A., Kefala, K., & Tennyson, J. 2024, MNRAS, 528, 3719
Zamyatina, M., Christie, D. A., Hébrard, E., et al. 2024, MNRAS, 529, 1776
Zhang, M., Hu, R., Inglis, J., et al. 2024, ApJL, 961, L44
Zieba, S., Kreidberg, L., Ducrot, E., et al. 2023, Natur, 620, 746